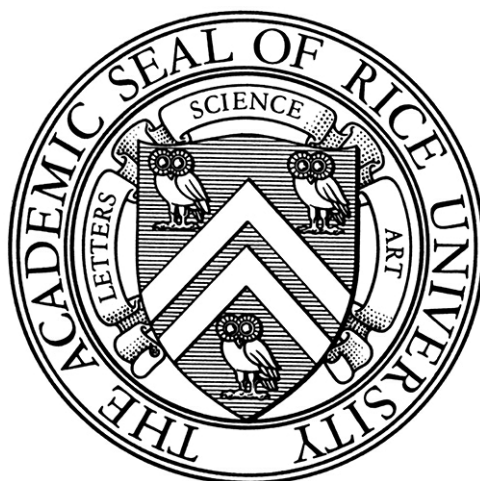


RICE UNIVERSITY



**A New Optical Trap System for  
Ultracold Strontium**

by

**Ying Huang**

**Master of Science**

Houston, Texas

August 16, 2013

RICE UNIVERSITY

**A New Optical Trap System for  
Ultracold Strontium**

by

**Ying Huang**

A THESIS SUBMITTED  
IN PARTIAL FULFILLMENT OF THE  
REQUIREMENTS FOR THE DEGREE

**Master of Science**

APPROVED, THESIS COMMITTEE:

---

Hulet, Randall G.  
Fayez Sarofim  
Professor of Physics and Astronomy

---

T. C. Killian, Chair  
Professor of Physics and Astronomy

---

Han Pu  
Associate Professor of Physics and  
Astronomy

Houston, Texas

May, 2013

# A New Optical Trap System for Ultracold Strontium

Ying Huang

## Abstract

Atoms can be trapped at the foci of intense laser beams, which can enable the study of interactions and dynamics of ultracold gases. In this thesis, we will describe our new trap designs. A large volume pancake-shaped optical dipole trap is initially used for loading large numbers of atoms from a Magneto-Optical Trap. A BEC with a large number of  $^{84}\text{Sr}$  atoms has been achieved after evaporation in this trap. To form degenerate gas of  $^{88}\text{Sr}$  we compress the mixture of  $^{88}\text{Sr}$  and  $^{87}\text{Sr}$  from the loading trap into a superimposed dimple trap. This combination improves the reproducibility of the experiment and shortens the time required to create quantum degenerate samples, while we are able to create  $^{88}\text{Sr}$  BEC with high density. In order to generate BEC of  $^{86}\text{Sr}$ , an isotope with large scattering length and extremely high three-body loss rate, we implement an optical sheet trap which has an aspect ratio of 1:10. The tight axis in the vertical direction provides strong potential to hold against gravity while the large horizontal dimension brings up the trap volume and keeps down the atomic density.

## Acknowledgments

Firstly I want to thank my advisor Dr. Thomas Killian, who always supports and encourages me to go through the darkness in research, who is always patient and considerate to his students. I'm so grateful to have you as my mentor. Then I will say thank you to all my group members, Mi Yan, Brian DeSalvo, Trevor Strickler, Patrick McQuillen, Francisco Camargo, Jim Aman and Thomas Langin, especially to Brian and Mi. I really appreciate doing research and talk about physics with you guys, and thank you for always standing by me. Finally I will thank my parents and friends. I love you all and nothing can be achieved without you.

# Contents

Abstract	ii
Acknowledgments	iii
List of Figures	vi
<b>1 Introduction</b>	<b>1</b>
1.1 Optical dipole trap . . . . .	2
1.2 Evaporative cooling . . . . .	6
<b>2 Large volume loading trap for efficient transfer of atoms and achieving <math>^{84}\text{Sr}</math> BEC</b>	<b>9</b>
2.1 Loading trap design . . . . .	10
2.1.1 Loading trap optical design . . . . .	10
2.1.2 Loading trap beam profiles . . . . .	14
2.1.3 Alignment of the loading trap beams . . . . .	14
2.1.4 Power locking system for loading trap . . . . .	15
2.2 Loading trap depth and effective volume . . . . .	18
2.3 Achieving $^{84}\text{Sr}$ condensate in the loading trap . . . . .	19

<b>3</b>	<b>Crossed-beam dimple trap to generate high density <math>^{88}\text{Sr}</math> BEC</b>	<b>22</b>
3.1	Dimple trap design . . . . .	22
3.1.1	Description of trap optical design and beam profiles . . . . .	22
3.1.2	Power locking system . . . . .	24
3.2	Trap frequency measurement and modeling of the dimple trap . . . . .	29
3.3	Achieving $^{88}\text{Sr}$ condensate in the dimple trap . . . . .	36
<b>4</b>	<b>High aspect radio sheet trap to produce <math>^{86}\text{Sr}</math> BEC</b>	<b>43</b>
4.1	Motivation to design an elongated optical trap for generation of $^{86}\text{Sr}$ BEC . . . . .	44
4.2	Description of trap design . . . . .	45
4.3	Achieving $^{86}\text{Sr}$ condensate in a sheet trap . . . . .	47
<b>5</b>	<b>Conclusion</b>	<b>52</b>
	<b>Bibliography</b>	<b>53</b>

# Figures

1.1	Energy diagram for $^{88}\text{Sr}$ . . . . .	2
1.2	Schematic diagram of evaporative cooling mechanism . . . . .	5
2.1	Optical layout of the loading trap. . . . .	10
2.2	Beam profile of 1064nm fiber laser after 5x Beam expander . . . . .	12
2.3	Loading trap beam profiles . . . . .	12
2.4	Numerical results of loading trap depth . . . . .	16
2.5	Effective volumes of the loading trap at different trap depth and temperature . . . . .	17
2.6	Loading curve in loading trap for $^{84}\text{Sr}$ . . . . .	21
2.7	Time-of-flight images of $^{84}\text{Sr}$ BEC . . . . .	21
3.1	Schematics drawing of dimple trap optical layout . . . . .	25
3.2	Dimple trap beam profiles . . . . .	25
3.3	Schematics of dimple trap power lock circuit. . . . .	27
3.4	Block diagram of dimple trap power locking system . . . . .	27

3.5	Group DC response versus input control voltage. . . . .	28
3.6	Group gain and phase shift in frequency spectrum . . . . .	28
3.7	Measured dimple trap number of atoms versus trap depth modulation frequency . . . . .	33
3.8	Fitting and experiment measurements of dimple trap frequency at different trap potential . . . . .	37
3.9	Numerical simulation of loading trap depth . . . . .	38
3.10	Diagrams of dimple trap power calibration . . . . .	39
3.11	Loading curve in dimple trap for $^{87}\text{Sr}$ . . . . .	40
3.12	Evaporation trajectory for $^{88}\text{Sr}$ in the optical dipole trap. . . . .	41
3.13	$^{88}\text{Sr}$ condensate time-of-flight absorption images. . . . .	41
3.14	Bimodal distribution fitting of $^{88}\text{Sr}$ thermal cloud and condensate. . . . .	42
4.1	Schematics drawing of sheet trap optical layout. . . . .	45
4.2	Profile of the first pass sheet trap beam . . . . .	46
4.3	Loading curve in the sheet trap for $^{86}\text{Sr}$ . . . . .	47
4.4	Atom numbers and temperature versus evaporation time for varies evaporation trajectory in the sheet trap for $^{86}\text{Sr}$ , where $\beta=1$ . . . . .	48
4.5	Evaporation trajectory to reach Bose-Einstein condensate of $^{86}\text{Sr}$ . . . . .	49
4.6	$^{86}\text{Sr}$ absorption images for different evaporation time. . . . .	50
4.7	Bimodal distribution fitting of $^{86}\text{Sr}$ thermal cloud and condensate . . . . .	50

4.8	Time-of-flight images of $^{86}\text{Sr}$ atom cloud after evaporation cooling.	51
-----	---	----

# Chapter 1

## Introduction

Quantum degenerate gases of divalent atoms have garnered substantial amount of interest in recent years. The two-valence-electron structure results in metastable excited states, which give rise to powerful narrow-intercombination line cooling [10], precise optical clocks [5], low loss optical Feshbach resonances [7], and efficient generation of long lifetime molecular systems [13]. In addition, the closed shell structure of group two atoms allows for applications in quantum computation and information [17]. Of particular interest to our lab are studies of ultracold collisional dynamics, photo-association properties, strong dissipative interactions in an optical lattice, and generation of highly correlated atom-molecular systems.

The lack of unpaired electrons in alkaline earth metal atoms makes an optical dipole trap (ODT) the only choice to perform efficient evaporative cooling. The design, implementation and characterization of three such traps make up the focus of this thesis. In this chapter, I will introduce the mechanism of an ODT and the scheme of evaporative cooling. Then I will discuss the collisional properties of all three Bosonic isotopes of Strontium and how the elastic and inelastic interactions affect the evaporation process. Finally I will give the outline of this thesis.

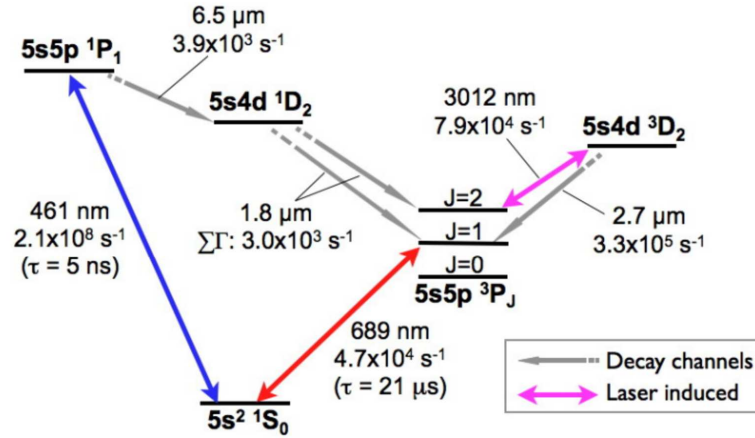


Figure 1.1 : Energy diagram for  $^{88}\text{Sr}$ . The transitions highlighted in blue and red are the principal transition (461nm, blue MOT) and narrow intercombination line (689nm, red MOT) transition for laser cooling of Sr respectively. The laser induced far-infrared transition repumps atoms that are magnetically trapped in the  $^3P_2$  state back to  $^1S_0$  through a decay channel.

## 1.1 Optical dipole trap

Evaporative cooling in an optical dipole trap has become a ubiquitous technique utilized in reaching quantum degeneracy of alkaline earth metal atoms. Lacking an electronic magnetic moment in the ground state forbids magnetic trapping of the atoms. Therefore a different trapping mechanism for evaporative cooling is required. The optical dipole trap used in our experiments is formed by a far red-detuned laser beam focused to high intensity on the atoms. The electric field of the laser  $\vec{E}$  induces an atomic dipole moment and the interaction of the induced dipole with the electric

Table 1.1 : Scattering length of stable Strontium isotopes [9]

Isotope	Abundance (%)	Scattering length a(a <sub>0</sub> )
<sup>84</sup> Sr	0.56	122.7(3)
<sup>86</sup> Sr	9.86	823(24)
<sup>88</sup> Sr	82.58	-1.4(6)
<sup>87</sup> Sr	7.0	96.2(1)
<sup>87</sup> Sr- <sup>88</sup> Sr	N.A.	55.0(2)

field leads to a potential energy  $U = -\bar{p} \cdot \bar{E}$ ,  $\bar{p} = -\alpha \bar{E}$ , where  $\bar{p}$  is the induced dipole moment and  $\alpha$  is the polarizability. This is known as the AC Stark shift. The field gradient resulting from the spatial Gaussian distribution of the laser intensity leads to a gradient of the potential and thus a force on the atoms known as the optical dipole force.

The atomic polarizability  $\alpha$  can be calculated from basic atomic physics [1]. The rotating-wave approximation requires  $|\Delta| \ll \omega_0$ , where  $\Delta \equiv \omega - \omega_0$  is the detuning between the resonant frequency  $\omega_0$  and the laser frequency  $\omega$ . In our experiment for the principal transition at 461nm, the resonance frequency is  $2\pi \times 6.42 \cdot 10^{15}$ Hz and the 1064nm laser frequency is  $2\pi \times 2.78 \cdot 10^{15}$ Hz, where  $\Delta = 2\pi \times 3.64 \cdot 10^{15}$ Hz. Even though  $|\Delta| \ll \omega_0$  is not satisfied, the neglected term, when making the rotating wave approximation, which is proportional to  $1/(\omega + \omega_0)$ , is much smaller than the kept term which is  $\propto 1/(\omega - \omega_0)$ . So the rotating wave approximation gives a good

understanding of how the ODT works.

The dipole potential in the trap is proportional to the laser intensity profile as

$$U_{dipole} = \frac{3\pi c^2}{2\omega_0^3} \frac{\Gamma}{\omega - \omega_0} I(r) \quad (1.1)$$

where  $\Gamma$  is the spontaneous emission decay rate from the excited state and  $I(r)$  is the field intensity [4].

The assumption we made here is that only one transition contributes to the optical dipole potential. This simple expression will be a good approximation because the 461nm line transition contributes the most to the potential for the ground state atoms. For a more accurate calculation, other levels including the continuum will contribute [12].

For red-detuned laser beam which is the case in our setup,  $\Delta < 0$  the atoms will feel a dipole force attracting them to the laser intensity maximum and will be trapped at the focus.

For a single beam dipole trap and the relatively large beam waist that we use for our ODT lasers, the confinement in the axial direction is much weaker than the radial axis and atoms tend to leak out of the trap longitudinally. To provide confinement along the axial direction of the dipole trap beam, we refocus the trap laser beam onto the waist of the first pass at almost normal angle to build up a crossed dipole trap configuration, which yields an extra confinement along the weak axis.

Even though the ODT laser is far detuned, atoms can still scatter real photons, which results in heating. The scattering rate of atoms is a crucial parameter to

characterize the property of an optical dipole trap, which for our conditions, is given by

$$\Gamma_{sc} = \frac{\Gamma}{\Delta\hbar} U_{dipole} \quad (1.2)$$

As the dipole potential scales as  $1/\Delta$  while the scattering rate goes as  $1/\Delta^2$ , it is feasible to trap atoms in an optical dipole trap if we have a relatively large detuning in the laser beam with respect to the closest resonance transition and large intensity. Then the trap dipole potential can be deep enough to trap atoms, while the scattering loss rate is small compared with other decay mechanisms in the trap.

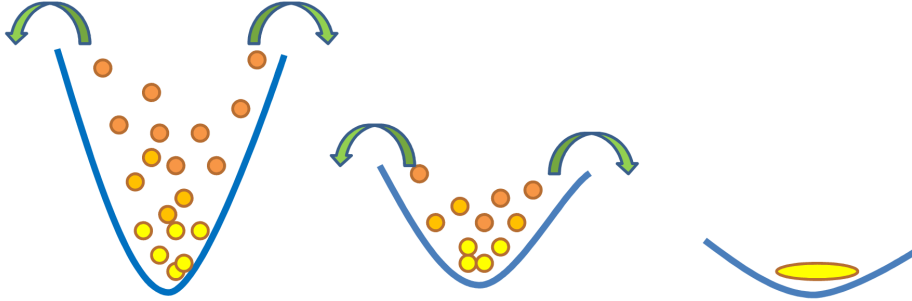


Figure 1.2 : Schematic diagram of evaporative cooling mechanism. Plot [A] is corresponding to the optical dipole trap with the deepest trap potential, where plain evaporation is processing. After the intensity of the trap laser beam has been lowered, the trap depth decreases and forced evaporation takes into play ([B]). In the end of evaporation shown in [C], we achieve quantum degenerate gas.

## 1.2 Evaporative cooling

In a conservative trap like an optical dipole trap, evaporative cooling is a very efficient way to increase the phase-space density of atoms and finally reach quantum degeneracy. The atoms with high kinetic energy will escape from the trap and the remaining atoms will thermalize subsequently due to elastic collision process. Figure 1.2 shows a simple schematics of how the evaporative cooling proceeds in our lab. After loading atoms into the optical dipole trap, we typically hold at maximum trap potential for hundreds of milliseconds for a plain evaporation (Figure 1.2 [A]). As the atoms left in the trap no longer have sufficient energy to escape from the deep potential, we decrease the laser power to lower the trap potential continuously and do forced evaporation (Figure 1.2 [B]). The most energetic atoms are rejected from the trap and carry away a large amount of thermal energy. This cooling, and associated density increase due to the trapping force, leads to increasing phase space density and eventual formation of a BEC.(Figure 1.2 [C]) [14].

Efficient evaporative cooling requires high elastic collision rate, which will promote the thermalization of atoms, and low inelastic collision rate, which leads to loss. One often speaks of a desire for a high ratio of good to bad collisions. In Sr, because the ground state is non-degenerate, there are no two-body loss process to be concerned about. Our main concerns are the background pressure, the ODT light scattering that leads to one-body loss, and three-body collisional losses. We see lifetimes in our ODT at low density of 30s due to one-body processes. This sets an upper limit on

the timescale of evaporative cooling and means we need high enough atom density and elastic collision rates to evaporate on a 10s timescale.

Different isotopes, with different scattering properties are more or less sensitive to these processes (Table 1.1). I will discuss them in the context of each isotope.  $^{84}\text{Sr}$  has a moderate scattering length of  $122.7a_0$  which will lead to high elastic rate, while the three-body scattering rate, which scales as  $a^4$  is tolerable. As I will show, in our new trap, we can easily load several millions of atoms in the ODT and get high enough collision rates to form BECs in a few seconds of evaporation [3]. As  $^{88}\text{Sr}$  has a small and negative scattering length ( $-2a_0$ ), it cannot thermalize efficiently in the trap. So we mix it with  $^{87}\text{Sr}$  and the inter species scattering length of  $55.2a_0$  is appropriate to achieve efficient sympathetic evaporative cooling for both isotopes [11]. For atoms with large scattering length like  $^{86}\text{Sr}$ , because the elastic collision rate is proportional to  $a^2n$ , and inelastic scattering rate scales as  $a^4n^2$ , where  $n$  is the density of atoms, we favor a low density of atoms to keep down the ratio between the two.

Another loss process which will influence the initial density of atoms loaded into the ODT is the photo-association process, which is going on during the overlap transfer stage from the 689nm red MOT into the optical trap. As the photo-association loss rate is proportional to the atomic density  $\dot{\gamma} = -K_1n$ , where  $K_1$  is the two-body loss rate, it does set a limit on the density in the ODT initially [21].

The focus of this thesis is the design and characterization for a series of three newly built optical dipole traps (ODTs) aimed at optimum evaporative cooling environment

for all three Bosonic isotopes of Sr individually. In order to create a large number of  $^{84}\text{Sr}$  BEC, we construct a large volume cigar-shaped optical trap (loading trap) which keeps down the atomic density during the transfer from the red MOT and loads three times more atoms compared with our previous ODT. For the purpose of achieving a high density profile of  $^{88}\text{Sr}$  BEC, we build an optical dipole trap with tight waist (dimple trap) which has a smaller trap volume than our old ODT design, and we successfully prepared  $^{88}\text{Sr}$  BEC with a peak density in the order of  $10^{15}\text{cm}^{-3}$ . As mentioned earlier, a low density of  $^{86}\text{Sr}$  is required during evaporation in order to reduce the three-body inelastic loss rate, so we design a high aspect-ratio sheet-shaped optical trap (sheet trap) and observed the first  $^{86}\text{Sr}$  BEC in our lab. I will skip introductions to the complete experiment apparatus and trapping and cooling proceed to reaching quantum degeneracy [3].

## Chapter 2

### Large volume loading trap for efficient transfer of atoms and achieving $^{84}\text{Sr}$ BEC

In 2009-2011 we achieved the first BEC of  $^{84}\text{Sr}$  [10] simultaneously with the Innsbruck group [18], the first quantum degenerate Fermi gas of  $^{87}\text{Sr}$  [15], and the first BEC of  $^{88}\text{Sr}$  [11] in our old spherical optical dipole trap (ODT) which had a beam waist of  $90\mu\text{m}$ . In order to increase the number of atoms in the ODT and improve reproducibility for all experiments, we implemented a pancake-shaped optical trap (loading trap) with  $60\mu\text{m}$  waist vertically and  $300\mu\text{m}$  waist horizontally. The loading trap has a larger effective volume compared with our old optical dipole trap, and its cylindrical shape matches the spatial distribution of the  $689\text{nm}$  magnetic-optic trap (red MOT) which tends to have an elliptical geometry. As a result we successfully load three times more atoms from the red MOT into the optical trap than before. For  $^{88}\text{Sr}$ ,  $^{87}\text{Sr}$  and  $^{86}\text{Sr}$  we evaporate into secondary ODT configurations tailored to the collision properties of those isotopes. Evaporation in this trap can be very efficient for  $^{84}\text{Sr}$ . We can evaporate directly to BEC for  $^{84}\text{Sr}$ . The pancake-shaped geometry allows the trap to evaporate down to a shallow depth but can still hold against gravity in the vertical axis.

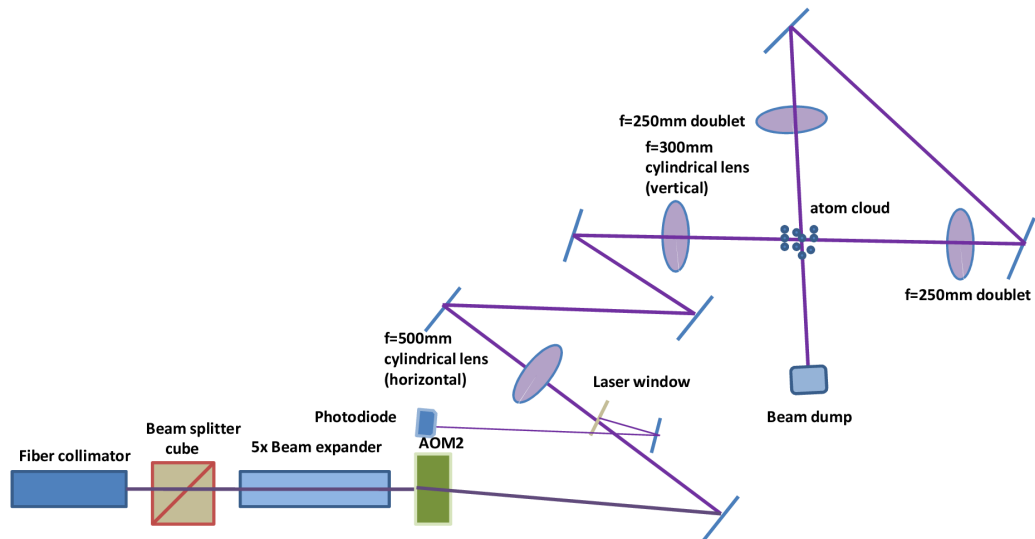


Figure 2.1 : Optical layout of the loading trap.

## 2.1 Loading trap design

### 2.1.1 Loading trap optical design

We generate our loading trap from an 18W, 1064nm, linearly-polarized multi-mode fiber laser (IPG Photonics), whose output is a collimated beam with  $1/e^2$  radius as  $2000\mu\text{m}$ . First the beam goes through a polarizing beam splitter to clean up the polarization (Figure 2.1). It then passes through a 5x beam expander (Thorlabs ELQ-25-5X-1064) with adjustable focus, which is oriented so as to compress the beam by about 5x and gives us flexibility for the optical design. An acoustic-optic modulator immediately after the expander (AOM1) is used to generate the beam for the dimple

trap configuration discussed in the next chapter and is omitted from the figure 2.1. The zeroth order beam from AOM1 propagates through AOM2, which generates the diffracted beam exploited for the loading trap beam. The distance needed to separate the zeroth and the deflected beams of the AOM is at least 27cm and our pick-off mirror is placed at the limit to save space. To reduce the thermal effect on optics as much as possible, we choose fused silica as the material for all the lenses and laser windows in the beam path. Unlike our former optical dipole trap laser beams [3] which were inclined by 10.5 degrees to horizontal plane in order to pass through dedicated ODT ports, the loading trap beam passes through MOT viewports horizontally in north-south direction then recycles back to cross itself in east-west direction. As the chamber windows are not designed for 1064nm laser transmission, the reflection loss is not negligible (30%). To aid alignment, we replace our MOT mirror by a 'hot mirror' that transmits 1064nm and reflects visible light. As our chamber center is 12" above the table surface, all the optical components for the first arm of the loading trap configurations are placed on a 24"  $\times$  48"  $\times$  0.5" solid aluminum breadboard which is raised by 8" from the main optical table. It is very convenient now to use standard 3" pillars for the optics on the raised platform rather than very long posts.

Practically the limitation of optical layout for the loading trap comes from the geometry of the vacuum chamber and space on the platform. For instance, the distance from the center of the chamber to the last optics cannot be less than 30cm,

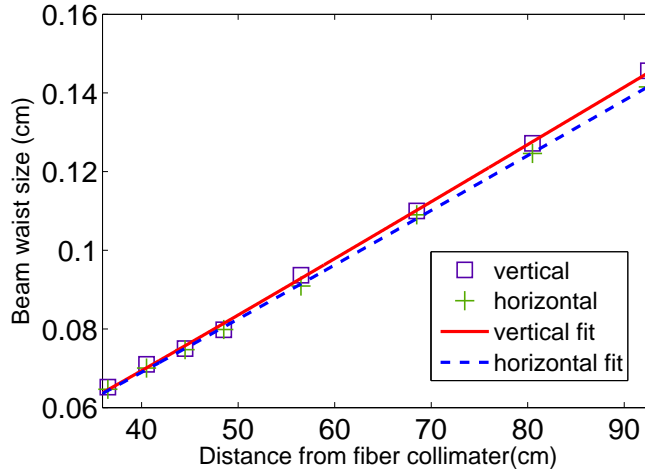


Figure 2.2 : Beam profile of 1064nm fiber laser after 5x Beam expander. The horizontal fit waist is  $237.54\mu\text{m}$  at  $-5.4\text{cm}$  and the vertical fit waist is  $228.52\mu\text{m}$  at  $-4.2\text{cm}$ . Origin is at the fiber collimator output front.

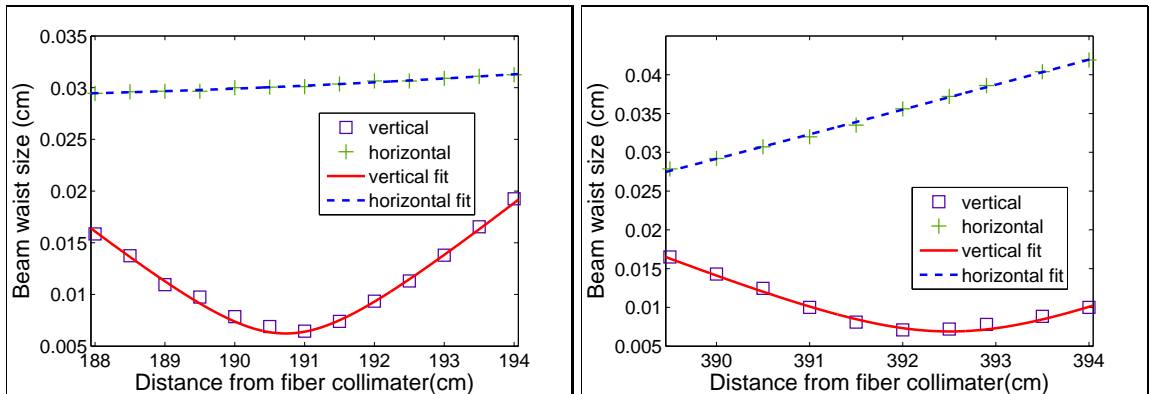


Figure 2.3 : Loading trap beam profiles. The profile on the left illustrates the measured  $1/e^2$ -radius (square and cross symbols) and the gaussian beam fittings (solid and dashed lines) of the first pass of the loading trap beam, while the right one is related to the return trap beam. For the first arm loading beam, the horizontal fit waist is  $291.89\mu\text{m}$  at  $184.13\text{cm}$  and the vertical fit waist is  $62.28\mu\text{m}$  at  $190.73\text{cm}$ . For the second arm loading beam, the horizontal fit waist is  $101.76\mu\text{m}$  at  $381.79\text{cm}$  and the vertical fit waist is  $68.63\mu\text{m}$  at  $392.50\text{cm}$ . Origins are at the fiber collimator output front. The atoms are suppose to locate at  $191\text{cm}$  for the first pass of the trap beam, and  $391\text{cm}$  for the second path.

and the platform extends out 50" with respect to the chamber. Taking these conditions into consideration, we adjust the beam expander to yield a  $230\mu\text{m}$  radius at the origin at the fiber collimator output front (profile see Figure 2.2). To generate a reasonably tight vertical waist at the atoms, we locate a cylindrical lens for the horizontal confinement with focal length of 500mm at 81cm and another one with  $f=300\text{mm}$  at 154cm away from the fiber collimator. We placed the last cylindrical lens on a one-axis translation stage that allows us to fine tune the vertical position of the waist. Because we plan to install optical lattice beams close to co-propagating with the loading trap beams, we try to align the trap beams so they are as close to normal as possible. We are limited in this regard by the need to separate the ODT beams from the MOT beams.

To refocus the returned beam crossed on the incident beam waist we implement an 8-f (focal length) imaging system on another raised platform at the same height as the first aluminum breadboard, where the distances between the object and the first lens, the first lens and the second identical lens, and the second lens to the image are  $2\times f$ ,  $4\times f$  and  $2\times f$  respectively. The advantage of this optical imaging system is that it will project the object to the image with no magnification or distortion ideally, and force the image to move in the exactly same way as the object if there is any drift in its position, therefore once the two beams overlap they will stay crossed if we slightly adjust the optics in the first pass for a better alignment. In our configuration we choose achromatic doublet lens pairs with focal length as 250mm to form this

imaging setup where the relative distance between the two waists is 2m. Then the atoms locate at 191cm for the first pass of the trap beam, and 391cm for the second path. All the measurements of absolute distances discussed in this chapter have the same origin at the fiber collimator output edge.

### 2.1.2 Loading trap beam profiles

Figure 2.3 illustrates the typical loading trap beam profiles for both the incident and the return trap beams. The Gaussian-beam propagation fitting of the measured profile data shows that, for the first arm loading trap, the horizontal waist size is  $292\mu\text{m}$  located at 184cm to the fiber collimator, and the vertical waist size is  $62\mu\text{m}$  at 191cm; for the second arm, the horizontal waist is  $102\mu\text{m}$  at 393cm and vertical waist is  $102\mu\text{m}$  at 382cm. The most critical geometric parameters of the trap beams are in the vertical axis and they matches our expectation quite well. For the horizontal axis that the trap characteristics are less sensitive. Even though the waist locations are off with respect to the center of the chamber by about 10cm, it is still within one Rayleigh range ( $Z_R = \pi\omega_0^2/\lambda=26.6\text{cm}$ , where  $\omega_0$  is the waist size and  $\lambda$  is the wavelength) and will work just fine.

### 2.1.3 Alignment of the loading trap beams

To align the single path loading beam on atoms from scratch, we send the first beam through the chamber by centering the beam on both windows horizontally and vertically, then slightly rotate the laser beam horizontally with respect to the center

of the chamber to leave path for the MOT beam. By tuning the magnetic field of the trim coil we are able to move the red MOT around and find the first pass of the beam. As the atoms expand very quickly in the shallow direction of the trap, we tweak the alignment of the loading beam to ensure the mass center of atoms stays stationary during expansion. We also fine rotate the cylindrical lenses to make sure the pancake-shaped beam is exactly horizontally oriented. It is more tricky to look for the second arm of the trap beam, as the searching method adapted for the first pass is not available any more. We made use of atom loss as a sensitive indicator of laser-atom overlap by implementing a diagnostic photo-association laser(PAS) beam. Firstly we aligned a large size PAS beam with high intensity tuned to be on resonance of transition  $^1S_0$ - $^3P_1$  on top of atoms, then we gradually dropped the intensity and shifted the detuning from resonance to be more sensitive to alignment. As the PAS beam is the output of a fiber with an adjustable output collimator, we can also adjust the focus to reduce the size of the beam to be more sensitive to the overlap of laser and atoms. After we are confident that the PAS beam was on the top of the atoms precisely, we try to overlap the second arm of the loading trap beam with the PAS beam.

#### **2.1.4 Power locking system for loading trap**

In order to minimize the laser intensity noise and control the trap depth, we apply a close loop servo to our laser system which will adjust the power of the diffracted

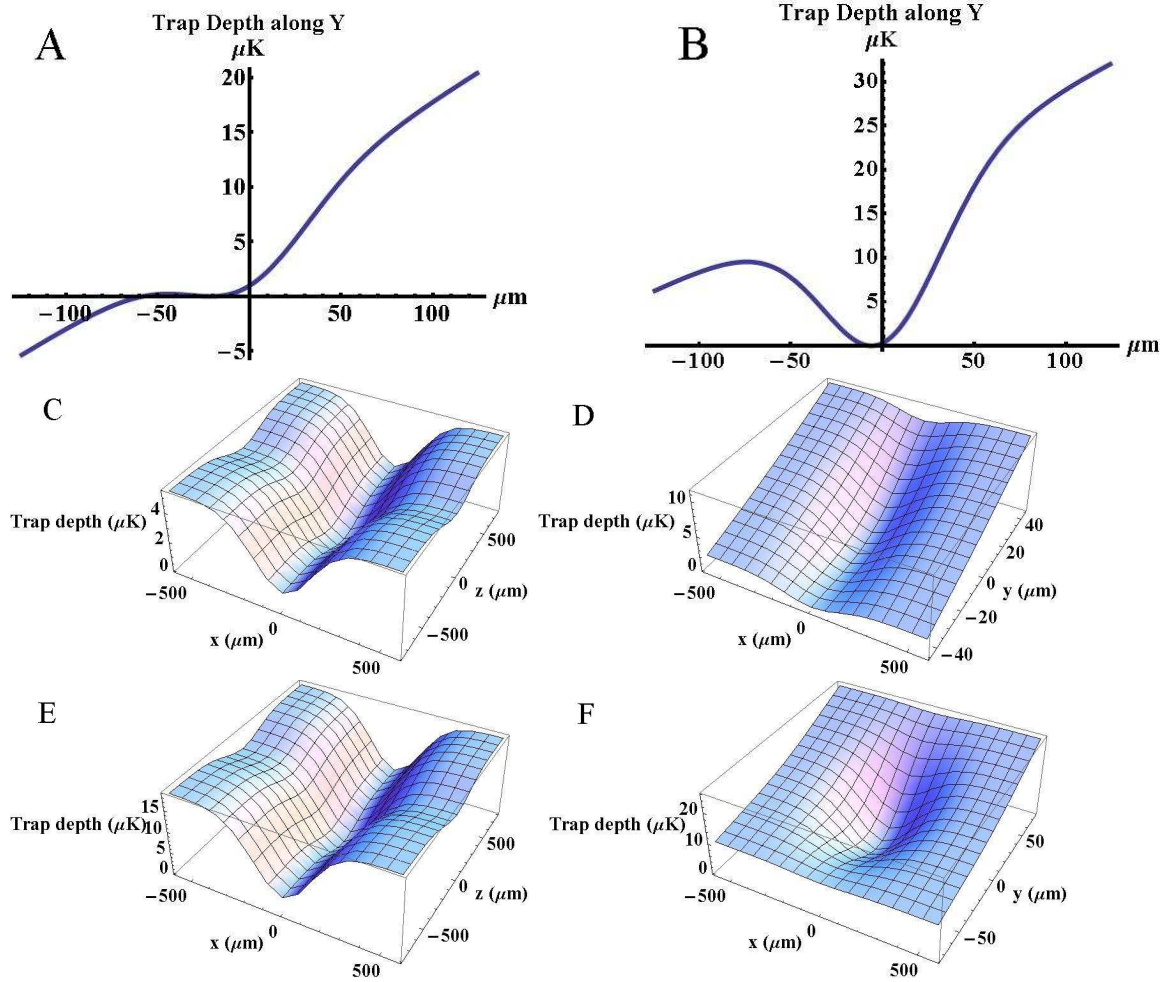


Figure 2.4 : Numerical results of loading trap depth. In the calculation the laser beam waists are taken from profile results. [A] and [B] present the trap potentials in gravity axis (Y) versus displacement in horizontal direction for both shallow trap (2.9V) and deep trap (8.5V); [C] and [D] show the 3D plots of 2.9V trap depth in vertical (y) and horizontal direction(z), while [E] and [F] are the related trap depth plots for 8.5V trap.

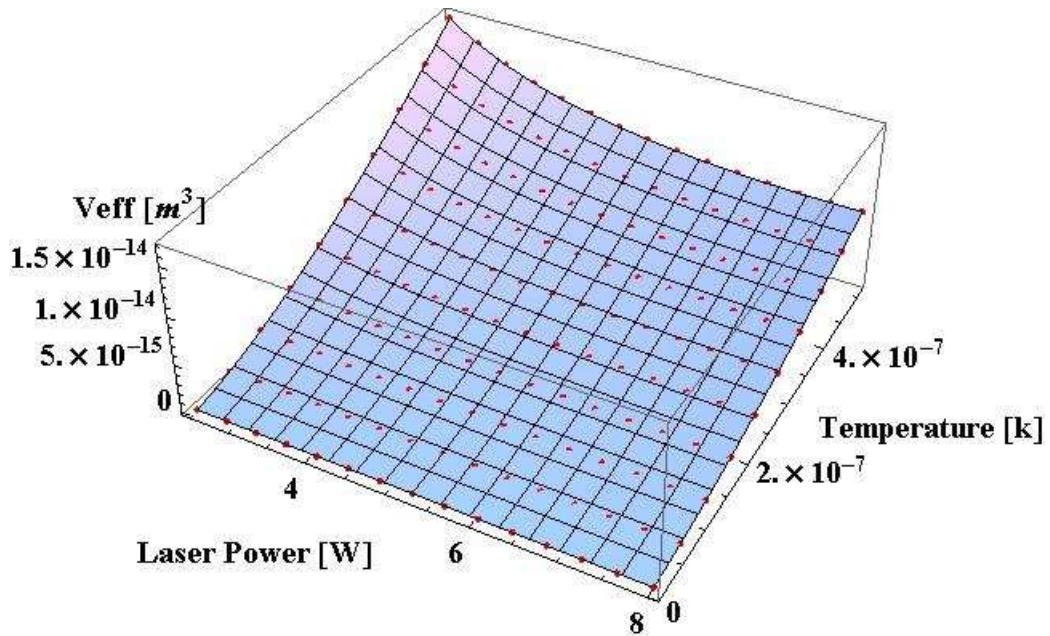


Figure 2.5 : Effective volumes of the loading trap at different trap depth and temperature.

beam of the AOM to match a set point, by controlling the radiofrequency (RF) power that generates the diffracted beam from the acoustic-optic crystal.

The locking system consists of a photodiode monitor that detects the beam power dynamically (Figure 2.1), a locking circuit that contains the reference voltage, the summing junction and gain stages, an analog control RF source and an AOM. We attached a bandpass filter for 1064nm on the photodiode detector and also shield it to yield the minimum effect from stray light. Now we are able to perform the evaporation trajectory in a precisely controlled way and lock out noise up to the bandwidth of the locking system (about 80KHz). More details of the power locking circuit can be found in the next chapter.

The power controlled voltage for the trap beam has a full range of 0-10V, which is corresponding to 0-14W laser power before entering the chamber (conversion factor=1.4W/V). Another factor that needs to be taken into account when calibrating the trap power on atoms is the transmission of the chamber windows for 1064nm laser (70%). The first arm passes the chamber window once while the second arm goes through two more windows. So if we set the reference voltage of laser beam at 5V, the actual power of the first pass beam at atoms will be  $5 \times 1.4 \times 0.7 = 4.9W$  and the power of the second pass is  $4.9 \times 0.7^2 = 2.4W$ .

## 2.2 Loading trap depth and effective volume

To optimize the forced evaporative cooling procedure in the new trap, we numerically simulate the dynamics of  $^{84}\text{Sr}$  in the loading trap and calculate its physical characteristics by the collisional model described in Ref [22]. Figure 2.4 demonstrates the trap potentials along the gravity direction (Y) for both deep trap (8.5V) and shallow trap (2.9V). The gravity sagging plays a more important role at low trap depth as the tilt of the vertical potential is enhanced. The 8.5V and 2.9V traps have the depth of  $\text{kB} \times 3.5\mu\text{K}$  and  $\text{kB} \times 0.2\mu\text{K}$  respectively, and the trap frequencies are  $f_y=205\text{Hz}$ ,  $f_x=42\text{Hz}$  and  $f_z=15\text{Hz}$  for the deep trap and  $f_y=83\text{Hz}$ ,  $f_x=23\text{Hz}$  and  $f_z=9\text{Hz}$  for the shallow trap.

Once we measured the total atom number at certain temperature, we can relate it to the peak atomic density by  $n_0 = N/V_{eff}$ , where N is the total number of atoms.

The atom number in the trap has an expression as  $N = \int n_0 d^3r f(r)$ , where  $n_0$  is the peak density,  $f(r)$  is the normalized density distribution. We define the effective volume as  $V_{eff} = N/n_0$ . The model appropriate to calculate the trap effective volume depends on the value of  $\eta$ , where  $\eta$  equals the ratio between trap depth and the atom cloud temperature  $k_B T$ . Due to the collisional property of  $^{84}\text{Sr}$ ,  $\eta$  is around 10 in our experiment, which is in the high- $\eta$  ( $\eta > 4$ ) regime [22]. This allows us to use a very simple analytical model to mimic the evolution of atoms in the trap, as  $V_{eff} = \left(\frac{2\pi k_B T}{m\omega^2}\right)^{3/2}$ , where  $\omega$  is the geometric mean trap frequency. Figure 2.5 shows the effective volumes at different temperature for deep and shallow traps. Once we measured the total atom number at certain temperature, we can relate it to the atomic density.

### 2.3 Achieving $^{84}\text{Sr}$ condensate in the loading trap

I now will give very brief description of the procedure to generate  $^{84}\text{Sr}$  condensate in this trap, together with some experiment details for archiving. In the end I will show that we observed a large BEC of  $^{84}\text{Sr}$ .

Typically we are able to load  $16 \times 10^6$   $^{84}\text{Sr}$  atoms into the 461nm MOT (blue MOT) for 5s loading time, and  $48 \times 10^6$  atoms for 30s (Figure 2.6). The transfer efficiency from the blue to red MOT is about 50%, where we achieved  $9.4 \times 10^6$  atoms in the red MOT with a temperature of  $3\mu\text{K}$  for 5s loading, and  $23 \times 10^6$  atoms for 30s loading. The loading efficiency is up to 40% from the red MOT into the loading trap and we

observed  $3.2 \times 10^6$  atoms in the loading trap for 5s loading and  $9.4 \times 10^6$  atoms for full 30s loading. The lifetime of the trap is  $31.8 \pm 5.5$ s.

In order to generate quantum a degenerate gas of  $^{84}\text{Sr}$  in the loading trap, we load  $^{84}\text{Sr}$  atoms into the blue MOT for 10s, and further cool and compress in the red MOT for 200ms, and then transfer from the red MOT stage into the optical trap for 100ms. We optimized the red MOT parameters during this 100ms overlap time with the loading trap as it will affect the transfer efficiency and the final forced evaporation procedure significantly. Finally we perform the evaporation trajectory as  $V = V_1 / (1 + (t/\tau))^\beta + V_2$ , where  $\tau=2$ s,  $\beta = 1.4$ , and  $V_1=7$ V,  $V_2=3$ V for a time of 5s. Figure 2.7 presents the absorption images of  $^{84}\text{Sr}$  atomic cloud after full evaporation time at different drop times, and no discernible thermal wings are shown, while the distinct change in the aspect ratio of the cloud provides a direct proof of generation of condensate in a cylindrical trap. We fit the Bose-Einstein condensate of  $^{84}\text{Sr}$  using Gaussian function and it yields about  $1 \times 10^6$  atoms in the BEC, which is at least 4 times more than what we achieved earlier.

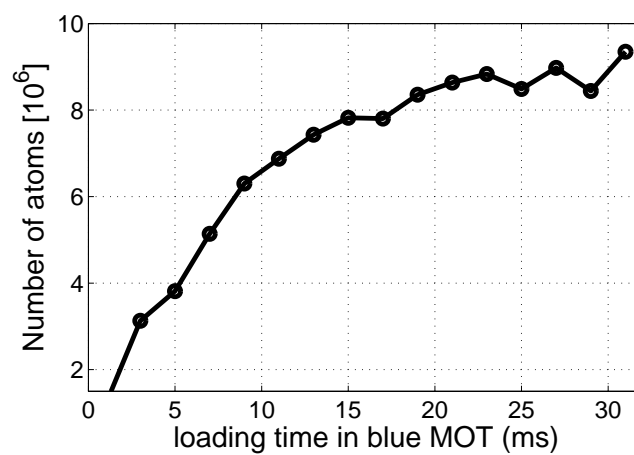


Figure 2.6 : Loading curve in loading trap for  $^{84}\text{Sr}$ , where horizontal axis is the loading time in blue MOT, and vertical axis is the number of atoms transferred into the loading trap.

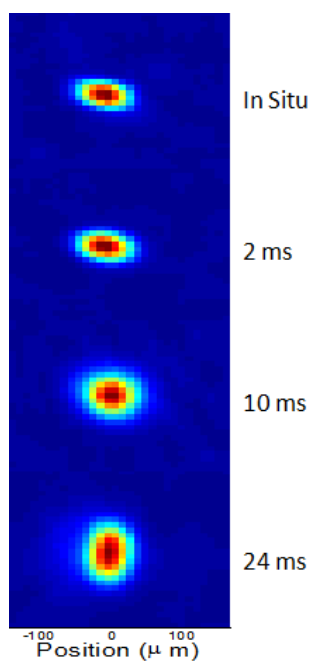


Figure 2.7 : Time-of-flight images of  $^{84}\text{Sr}$  BEC

## Chapter 3

### Crossed-beam dimple trap to generate high density $^{88}\text{Sr}$ BEC

In this chapter, I will describe our new optical dimple trap in which we sympathetically cool a mixture of  $^{88}\text{Sr}$  and  $^{87}\text{Sr}$  atoms transferred from the loading trap. This allows us to achieve Bose-Einstein condensation of  $^{88}\text{Sr}$ . Firstly I will give information about the fundamental optical layout for the dimple trap and show the beam profiles for both the incident and returned beams. Then I will talk about the trap power locking system which is important for stabilization and controlling the trap potential. In order to characterize our traps, we measured the trap oscillation frequencies and also calculated the trap potential from measured laser beam parameters and knowledge of the atomic polarizability. Finally I will briefly present the experimental proof to show we successfully create a high-density Bose-Einstein condensate of  $^{88}\text{Sr}$ .

### 3.1 Dimple trap design

#### 3.1.1 Description of trap optical design and beam profiles

The optical setup of the crossed-beam dimple trap was built on the same platform and shares the 1064nm laser source as the loading trap. A disadvantage of our old optical dipole trap [3] with a beam waist of  $90\mu\text{m}$  is that as Strontium has high

atomic mass and gravity is a significant issue. It is hard to control our old trap at low trap depths because of the tendency of gravity to dump the atoms out of the trap. In the new design we shoot for  $60\mu\text{m}$  waists in the radial axis to yield a tighter confinement and higher density for more efficient evaporation for the creation of BEC of isotopes that can tolerate high density. Figure 3.1 represents the optical layout for the dimple trap design. The setup before the acoustic-optic modulator (IntraAction Inc. ATM-802DA68) is the same as the loading trap. The output of the expander results in a waist of  $230\mu\text{m}$  at  $z=-4\text{cm}$  from the output edge of the fiber output. We use the diffracted order of the AOM1 as the optical source for the dimple trap, which allows us to control the turn on/off of the trap on a short timescale and modulate the trap laser power by managing the acoustic wave power. One concern of using the deflected beam from the AOM as the trap beam is that the thermal effect on the acoustic-optic crystal might distort the beam, so we choose the material as Tellurium dioxide which has a relatively low coefficient of thermal expansion.

We focus the diffracted beam from AOM1 by an achromatic doublet lens with a focal length of 250mm to minimize the effect of aberration. The lens is placed at  $z=113\text{cm}$  which is predicted to form a waist of  $60\mu\text{m}$  at  $z=147.5\text{cm}$ . Figure 3.2 shows the measured dimple trap beam profiles using the Beam Master profiler (Coherent inc.). We measured a horizontal waist of  $66.36\mu\text{m}$  at  $z=147.7\text{cm}$  and a vertical waist of  $69.62\mu\text{m}$  at  $147.58\text{cm}$ . For best performance we placed the lens with the surface with the smallest radius of curvature towards the incident quasi-collimated beam. For

fine alignment of the beam on atoms we added a computer controlled stepper-motor actuator (pico-motor<sup>TM</sup> New Focus) on a mirror mount before the beam goes into the chamber (Figure 3.1). The windows the dimple trap beams go through are designed for 1064nm, so the transmission is about 90%. To generate a crossed-beam dimple trap, we recycle the beam after the first transmission through the chamber in a 4-f imaging configuration, i.e. a first  $f=400\text{mm}$  lens is at 400mm away from the object (the waist of the incident beam), and a second  $f=400\text{mm}$  lens is at twice the focal length away from the first lens, then the waist will be 400mm away from the second lens. The advantage of the 4-f configuration is that the waist size is not sensitive to the distance between the two  $f=400\text{mm}$  lenses and we are able to translate the last lens in the beam propagation direction to place the waist on the atom. However, the location of the waist of the return beam will move in the opposite direction if there is any fluctuation in location of the first waist. The waist of the first pass of the trap beam locates at 147.5cm, and the second path locates at 307.5cm, where all the absolute distances discussed here have the origin at the fiber collimator output edge.

### 3.1.2 Power locking system

In order to stabilize the laser power and manage the trap depth in a controlled manner, we implement a power locking circuit in a closed servo system with a diagram shown in Figure 3.3. We are using a bare diode as the laser power monitor and build in a transimpedance amplifier to convert the detected photocurrent into voltage. Then

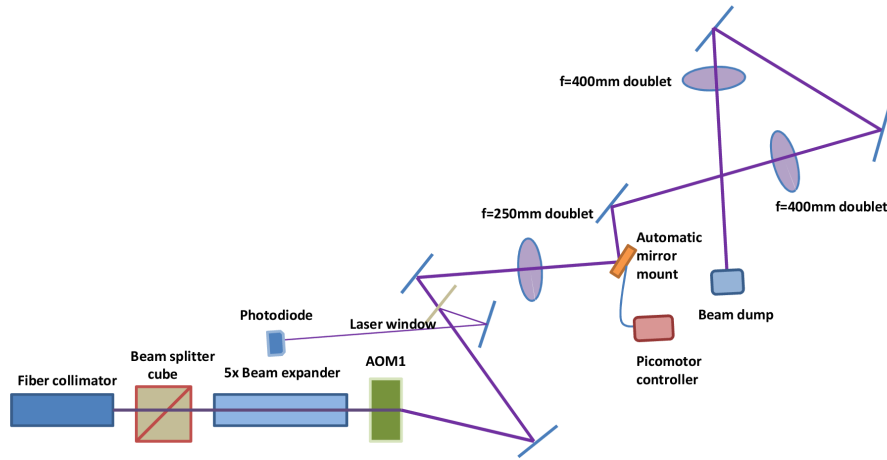


Figure 3.1 : Schematics drawing of dimple trap optical layout. The chamber is not shown here, while the atoms locate at the intersection of the crossing laser beams on the up-right corner of the figure.

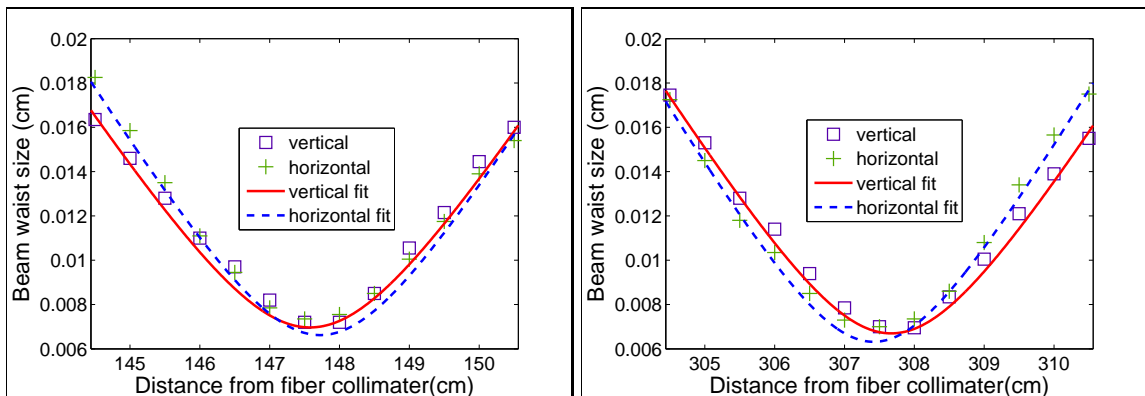


Figure 3.2 : Dimple trap beam profiles. The left figure shows the experiment data (square and cross symbols) and gaussian beam fitting (solid and dashed lines) of the  $1/e^2$ -radius of the first pass dimple beam. The right one is related to the returned beam. For the first arm dimple beam, the horizontal fit waist is  $66.36\mu\text{m}$  at  $147.7\text{cm}$  and the vertical fit waist is  $69.62\mu\text{m}$  at  $147.58\text{cm}$ . For the second arm dimple beam, the horizontal fit waist is  $63.73\mu\text{m}$  at  $306.5\text{cm}$  and the vertical fit waist is  $67.72\mu\text{m}$  at  $306.8\text{cm}$ . The atoms for the first pass is expected to be at  $147.5\text{cm}$ , and at  $307.5\text{cm}$ . Origins are at the front edge of the fiber collimator.

the photodiode signal gets amplified by an adjustable gain stage and sent into the summing junction. The other input to the summing junction is the set voltage signal coming from the computer which has also been amplified by an operation-amplifier and sent to the other port on the summing junction. The output of the summing amplifier is the error signal with an adjustable amplification which is controlled by a trim pot. By adjusting the trim pot resistance we are able to increase the gain of the locking system until the output signal starts to oscillate. The amplified error signal goes through the integrator stage, which allows us to lock the laser power signal to the set voltage. In order to increase the gain of the lock circuit at low frequency, we build an extra boost stage right after the integrator. In order to rapidly turn off the laser, we add in an analog switch which is controlled by a digital trigger. It will be activated on a logic high trigger and will short both the integrator and the boost circuit, then the diffracted power is set to zero independent of the computer control voltage. A protecting circuit consisting of a zener diode and a voltage divider aims at limiting the maximum output voltage to prevent damaging the analog control input of the radio-frequency generator. A manual switch on the output allows us to choose between locking at certain voltage or running at full laser power for diagnosis.

We'd like to characterize the bandwidth of our locking system to understand how quickly we can modulate the laser intensity and estimate the influence of trap power fluctuation to our atoms which is beyond the lock bandwidth. The block diagram of our locking system is demonstrated in Figure 3.4. In the control theory, the 3dB

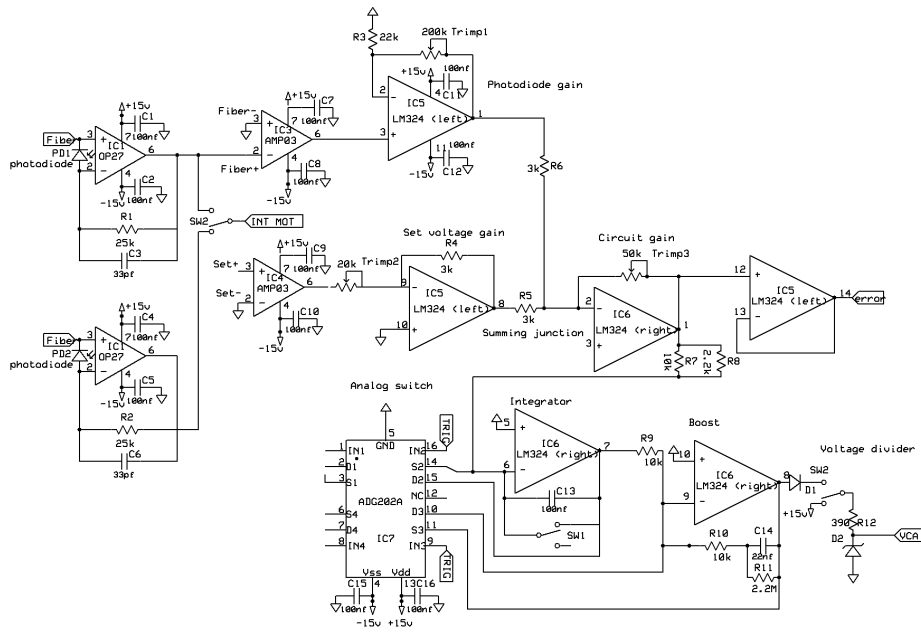


Figure 3.3 : Schematics of dimple trap power lock circuit.

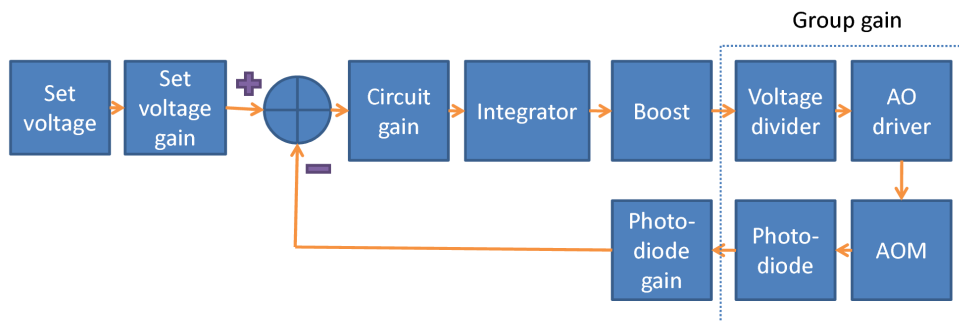


Figure 3.4 : Block diagram of dimple trap power locking system. It shows phases of inputs into the summing junction and the flow between each components in the feedback loop.

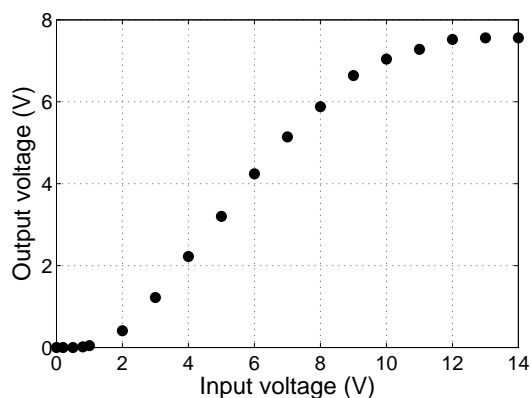


Figure 3.5 : Group DC response versus input control voltage.

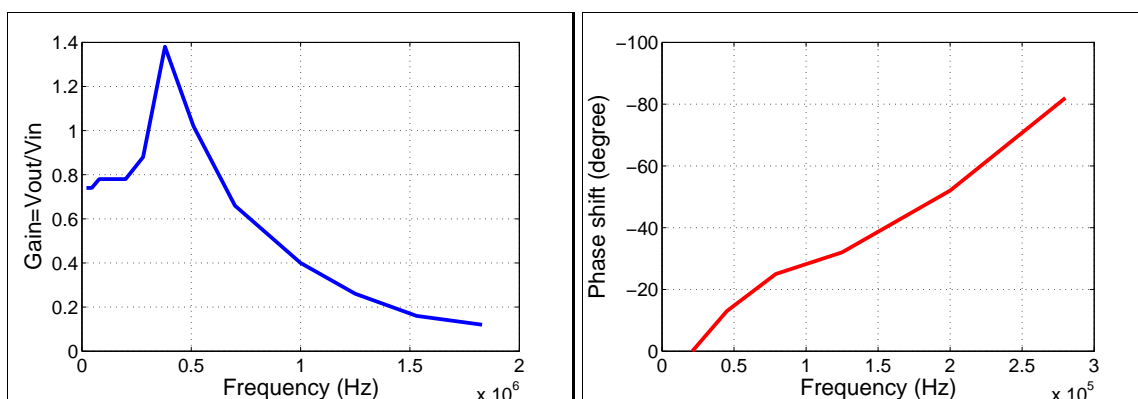


Figure 3.6 : Group gain and phase shift in frequency spectrum. We apply 2V offset voltage to the input and add in 300mV wiggle at each frequency for the measurements of the gain spectra.

frequency is where the product of the gains of all the individual components in the close-loop system reaches unity.

For convenience we lumped together hardware components including the voltage divider on the output of the lock circuit, the acoustic modulator driver (Isomet AO driver 533C-3-X), the acoustic-optic modulator and the photodiode monitor. The

gain of this lumped piece will be the ratio between the voltage converted from the photocurrent after the transimpedance amplifier and the voltage sent into the voltage divider. The gain properties of this grouped system in frequency domain will determine the limitation for the bandwidth of our power lock system. Figure 3.5 indicates that the DC response of the grouped components is nonlinear and the trap laser power will saturate at 12V input voltage. The non-ideal electronic property of the lumped system which deviates from a single-pole element assumption results in a high resonance peak in the gain amplitude spectra shown in Figure 3.6. In order to avoid oscillation of the laser power we want to limit the bandwidth of the locking system well below the resonance peak at 350KHz, at which the phase shift is already  $\pi/2$  of the grouped elements. We limit the unity gain bandwidth of the lock circuit to the order of 50-80 kHz. In fall 2012 we replaced the Isomet AO driver with an IntraAction light modulator signal processor (ME-803-24), which is expected to increase the bandwidth, but the amount of increase has not been quantified. The bandwidth analysis described here is related to the previous setup.

## **3.2 Trap frequency measurement and modeling of the dimple trap**

Most recently we did experiments on the coherent photo-association of  $^{88}\text{Sr}$  atom in a BEC in the dimple trap using the inter-combination transition. This yields a relatively long lifetime of the excited molecular state of  $10\mu\text{s}$ , as the decay rate of

a molecule is twice the rate of decay for a bare atom. The condition to reach the coherent regime can be set as  $\Omega = \omega_0 n_0^{1/2} \hbar \gg \gamma$ , where  $\Omega$  is the Rabi oscillation frequency of the BEC,  $\omega_0$  is the atom-molecular coupling constant,  $n_0$  is the BEC atomic density and  $\gamma$  is the incoherent loss rate [16]. In order to increase the BEC atomic density, we choose the isotope of  $^{88}\text{Sr}$  as our favored system, because its slightly negative scattering length ( $-2a_0$ ) induces attractive interaction in the BEC cloud and squeezes atoms to reach a higher peak density on the order of  $10^{15}\text{cm}^{-3}$  [11]. We also take advantage of the tighter confinement of our newly built dimple trap which also increases the atomic density. As the density profile of the BEC depends critically on the trap frequencies, it is very important to characterize our trap frequencies both experimentally and numerically.

Our dimple trap is formed by crossed gaussian laser beams, which have a spatial distribution as [3]

$$U(x, y, z) = \left[ \left( 1 + \left( \frac{\lambda z^2}{\pi \omega_x^2} \right) \left( \frac{\lambda z^2}{\pi \omega_y^2} \right) \right)^{-1/2} \exp \left( - \frac{2x^2}{\omega_x^2 \left( 1 + \frac{\lambda z^2}{\pi \omega_y^2} \right)} - \frac{2y^2}{\omega_y^2 \left( 1 + \frac{\lambda z^2}{\pi \omega_x^2} \right)} \right) \right] \quad (3.1)$$

where  $y$  is the close to the gravity direction. When modeling the trap potential, we take into account the 10.5 degree inclination of the trap beam from horizontal plane which will tilt the gravity potential  $U_g = mgy'$ , where  $g$  is the gravity acceleration and so that the  $y'$  axis is slightly angled with respect to  $y$ .

The trap can be approximated as a harmonic-oscillator and we did parametric excitation of atoms in the trap in order to extract the trap oscillation frequencies. We compress and release the trap potential periodically by modulating the laser

intensity at certain frequency. If the modulation frequency coincides with one of the atom vibrational frequencies in the trap multiplied by 2 over an integer [6], atom kicks synchronously and will gain energy. If the trap depth is much steeper than the average atomic energy, atoms will continuously gain kinetic energy and will be heated up but cannot escape from the trap, but no distinct atom loss signal will be observed. If the trap depth is not too high compared with the atomic thermal energy, atoms will be heated out of the trap, and we expect to see atom loss dips in our measurements. The competition between the evaporative cooling by rejecting the most energetic atoms out of the trap and the heating process by transferring the energy of parametric modulation of trap depth into the kinetic energy of atoms will determine whether we should see heating or cooling corresponding to the atom loss.

In the experiment, we apply a sinusoidal modulation to the trap laser intensity and sweep the modulating frequency for a cloud of thermal atoms. We expect to observe atom loss peaks and temperature spikes at frequencies of  $2f/n$ , where  $f$  is the resonant frequencies of the trap, and  $n=1,2,3\dots$ , which is referred to the second harmonic, fundamental and subharmonic oscillations respectively. The modulation intensity is 5% – 15% of the total trap beam intensity. The top two lines of plots in Figure 3.7 are the measured atom losses and temperature spectra for the 0.6V trap (0.65W power on the atoms in the first arm), which is approximately the trap depth at which we observe Bose-Einstein condensation of  $^{88}\text{Sr}$ . As the top two measurements

are both referred to the same trap potential but modulated at different intensity, it shows that by increasing modulation intensity it is possible to excite resonance modes with higher frequencies. The arrows on the top two figures point out four resonant frequencies related to the atom loss peaks at this trap depth. The bottom two figures are the trap frequency measurements for deeper traps (1.43V/1.53W trap for the third plot and 1V/1.08W trap for the last one), and we can recognize a trend that the trap frequencies shift with trap laser intensity.

In order to assign the measured trap frequencies to certain vibrational resonances of the trap and use the trap frequency measurements to constrain and confirm our knowledge of the trap, we calculated the exact 3D potential assuming a certain waist for both beams. We varied the waist as a fitting parameter to best fit the calculated trap frequencies to the measured atom loss peaks. We graphically show the trap potential for both shallow trap (0.6V/0.65W) and deep trap (1.43V/1.53W), where the trap depth are  $\text{kB} \times 1.57 \mu\text{K}$  and  $\text{kB} \times 7.38 \mu\text{K}$  (Figure 3.10). At deep trap depth, the effect of gravity is not dominant and the saddle points of the potential are along the horizontal direction. While in a shallow trap, gravity significantly alters the potential and the saddle point is along the gravity direction.

To extract the oscillation frequency from the calculation of the potential, we numerically fit a small region of the potential near the trap minimum to a 3D harmonic expression. There is a limitation to this method, as the actual trap potential is an inverted gaussian, which is anharmonic and only well approximated as parabolic near

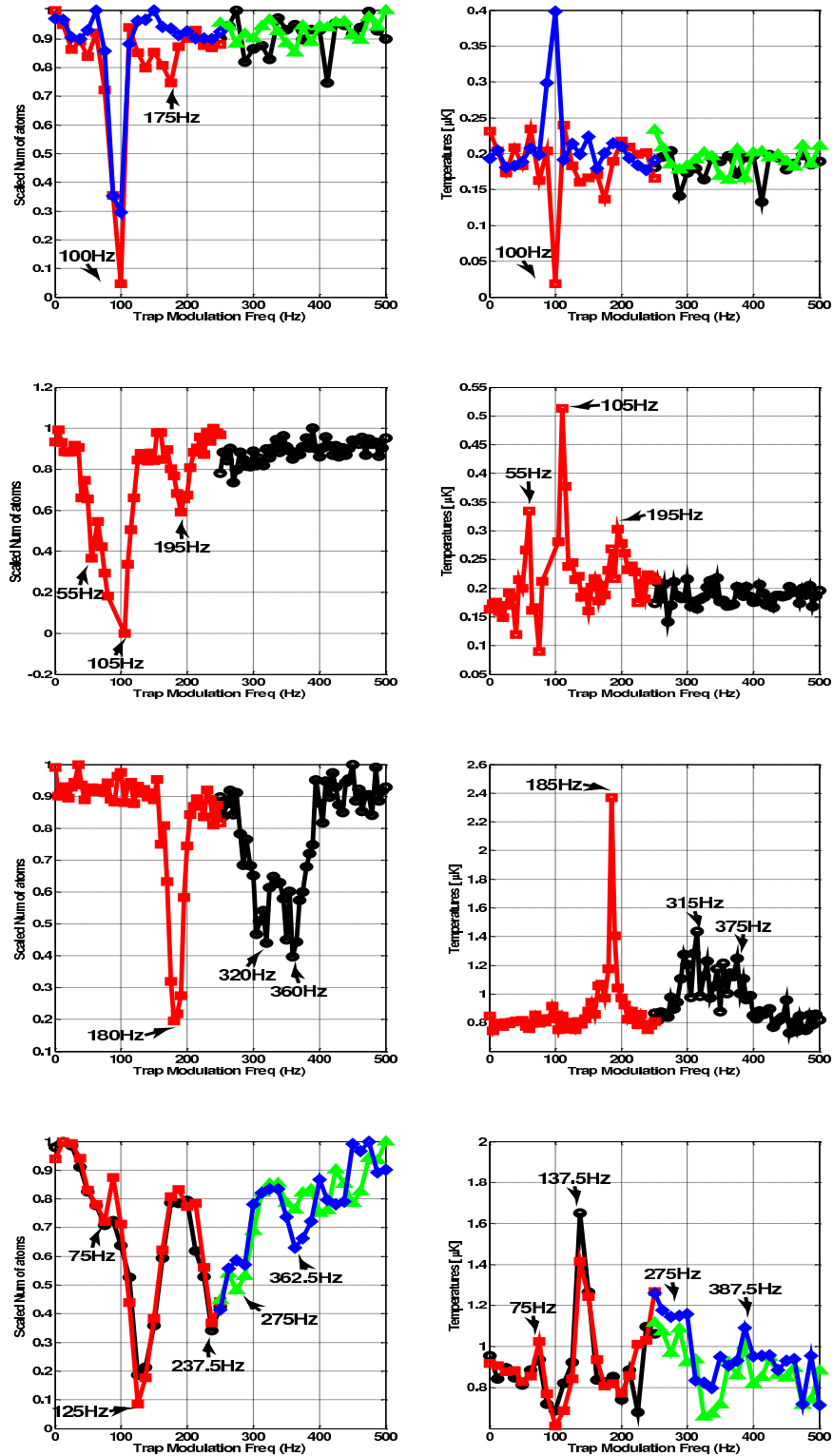


Figure 3.7 : Measured dimple trap number of atoms versus trap depth modulation frequency. Top one is 0.6V (0.65W) trap with 40mV modulation intensity in 0.5s interaction time for  $^{86}\text{Sr}$ ; the second top one is 0.6V (0.65W) trap with 120mV modulation intensity in 0.1s interaction time for  $^{86}\text{Sr}$ ; the third plot is 1.43V (1.53W) trap with 200mV modulation intensity in 0.1s interaction time for  $^{86}\text{Sr}$ ; the bottom plot is 1V (1.06W) trap with 200mV modulation intensity in 2s interaction time for  $^{87}\text{Sr}$ .

the trap minimum. In the limit of a very small region, our fit yields the frequency for small amplitude oscillation. The atoms, however, explore a larger region of the trap, and are sensitive to the anharmonicities, as

$$U(T) = \frac{1}{2}m\omega^2\sigma(T)^2 \quad (3.2)$$

where  $\omega$  is the trap oscillation frequency, and  $\sigma$  is the spatial extension of atoms from the minima of the trap to their thermal energy level. This introduces uncertainties and complications in our fitting procedure. To model the response of the atoms, we fit a larger region of the potential, up to a certain energy value, and the scale for this value is the thermal energy. We choose the atom energy to be  $0\%k_B T$ ,  $15\%k_B T$  and  $1/2k_B T$  respectively, and for the same trap, it gives  $5\% - 10\%$  uncertainty of the trap frequencies at low potential depth while  $10\% - 15\%$  variation at high trap potential. Even though most of atoms will be distributed at trap depth equal to the average energy of  $1/2k_B T$ , we decide to choose the energy of  $15\%k_B T$  as best guess fitting parameter because the atoms on the bottom of the trap are in the harmonic region and should respond more strongly to resonant excitation. In the measurement we choose the test isotope as  $^{86}\text{Sr}$  because its high elastic collision rate keeps the ratio between the trap depth and sample temperature at high values, and atoms are more localized in the harmonic region of the trap. We extract the best fitting waist of the trap laser beam by matching the simulated trap frequencies to the measured effective trap frequencies for thermal atoms. Then we can calculate the small amplitude oscillation frequencies seen by atoms in the BEC at the very bottom of the trap by plugging the

extracted waist size into the fitting procedure and setting the atom energy to  $0\%k_B T$ . While in principle it is possible to model this effect much more accurately than we have done, we have not pursued this. We account for this problem by assigning larger uncertainties to our measurements.

Figure 3.8 plots out the experiment measurements along with the calculated values of the fundamental and second harmonic trap frequencies. In the fitting procedure we assume a spherical trap beam and an equal waist size for both trap beams. We varied the guessed waist around our profiled waist in Figure 3.2, and the waist that gives the best fitting is  $66.5\mu\text{m}$ , which is a good match to the measured values from Figure 3.2. In Figure 3.8 it is clearly shown that the trap frequencies shift up with increasing trap potential. Even though we lack data points in the red solid curve which represents the fundamental excitation in the vertical axis, we detected signals in the second harmonic frequency corresponding to the gravity direction. There are two measured data points which have huge discrepancy to our fitting curves (below the black curve), we assigned these to the sub-harmonic excitations. While there is evidently some non-trivial dynamics at play affecting the coupling to different modes at different intensities and frequencies, the agreement between the measured values and our calculated values from the measure waists gives us confidence that our trap is well known.

As our trap frequency simulation procedure requires matrix symmetrization and diagonalization which is time-consuming, in order to simplify the process to extract

the trap frequency giving trap power, I fit the frequencies of the fundamental modes of the trap to hyperbolic functions  $a_1 \cdot e^{-a_2 \cdot p} + a_3 \cdot e^{a_4 \cdot p} + a_5$ , where  $a_i$  are coefficients,  $i=1,2,3,4,5$  (Table 3.1), and  $p$  is the laser power of the first arm on atoms.

Table 3.1 : Coefficients of hyperbolic functions by fitting the calculated fundamental modes of the dimple trap frequencies

Mode	$a_1$	$a_2$	$a_3$	$a_4$	$a_5$
Top branch	2757	-0.015	-163.2	-1.358	-2587
Middle branch	676.2	-0.035	-116.8	-0.926	-526.5
Bottom branch	1758	-0.015	-94.03	-1.148	-1640

### 3.3 Achieving $^{88}\text{Sr}$ condensate in the dimple trap

In the scope of demonstrating the generation of high density  $^{88}\text{Sr}$  BEC in the new dimple trap, I will briefly talk about our experimental procedures to reach quantum degeneracy, emphasizing the evaporative cooling scheme. I will provide some experimental details for record and future use.

As  $^{88}\text{Sr}$  has an s-wave scattering length very close to zero, it's impossible to perform efficient evaporative cooling as the elastic collision rate is proportional to  $a^2$  [19]. In order to achieve a quantum degenerate gas of  $^{88}\text{Sr}$ , we implement a combined trapping and cooling scheme of  $^{88}\text{Sr}$  and  $^{87}\text{Sr}$ , which has inter species s-wave scattering

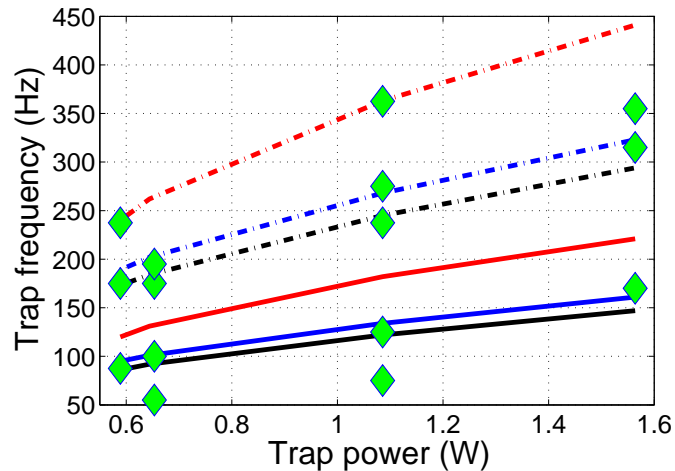


Figure 3.8 : Fitting and experiment measurements of dimple trap frequency at different trap potential, where the laser power of the first pass on atoms are 0.58W, 0.65W, 1.08W and 1.53W in sequence. The green diamonds are the experiment data of the trap frequencies partially extracted from Figure 3.7. The red, blue and black solid lines are the fitting for the first harmonic frequency branches, while the dashed lines are for the second harmonic excitations. We make an assumption that the beam is spherical with equal size in both the incident and returned trap beams. The two lowest frequency modes are not degenerate because of the 10.5 degree inclination of the trap beam plane to the horizontal plane. We fit the theory line to the data by assuming the atom energy in the trap is  $15\%k_B T$ .

length ( $55a_0$ ) favorable for effective sympathetic cooling of  $^{88}\text{Sr}$ .

As  $^{87}\text{Sr}$  is 10 times less abundant than  $^{88}\text{Sr}$ , to make this work, we focus on optimizing the transfer of  $^{87}\text{Sr}$  from the MOTs into the loading trap (Figure 3.11) and the lifetime of  $^{87}\text{Sr}$  in the loading trap is  $(19.1 \pm 2.1)s$ . Typically for 2s loading time, we will get  $42 \times 10^6$ ,  $17 \times 10^6$  and  $3.6 \times 10^6$  atoms into the blue MOT, the red MOT, and the loading trap in sequence. This takes into account the effect on absorption imaging calibration of optical pumping and variation in Clebsch-Gordon coefficients for different magnetic sublevels [12].

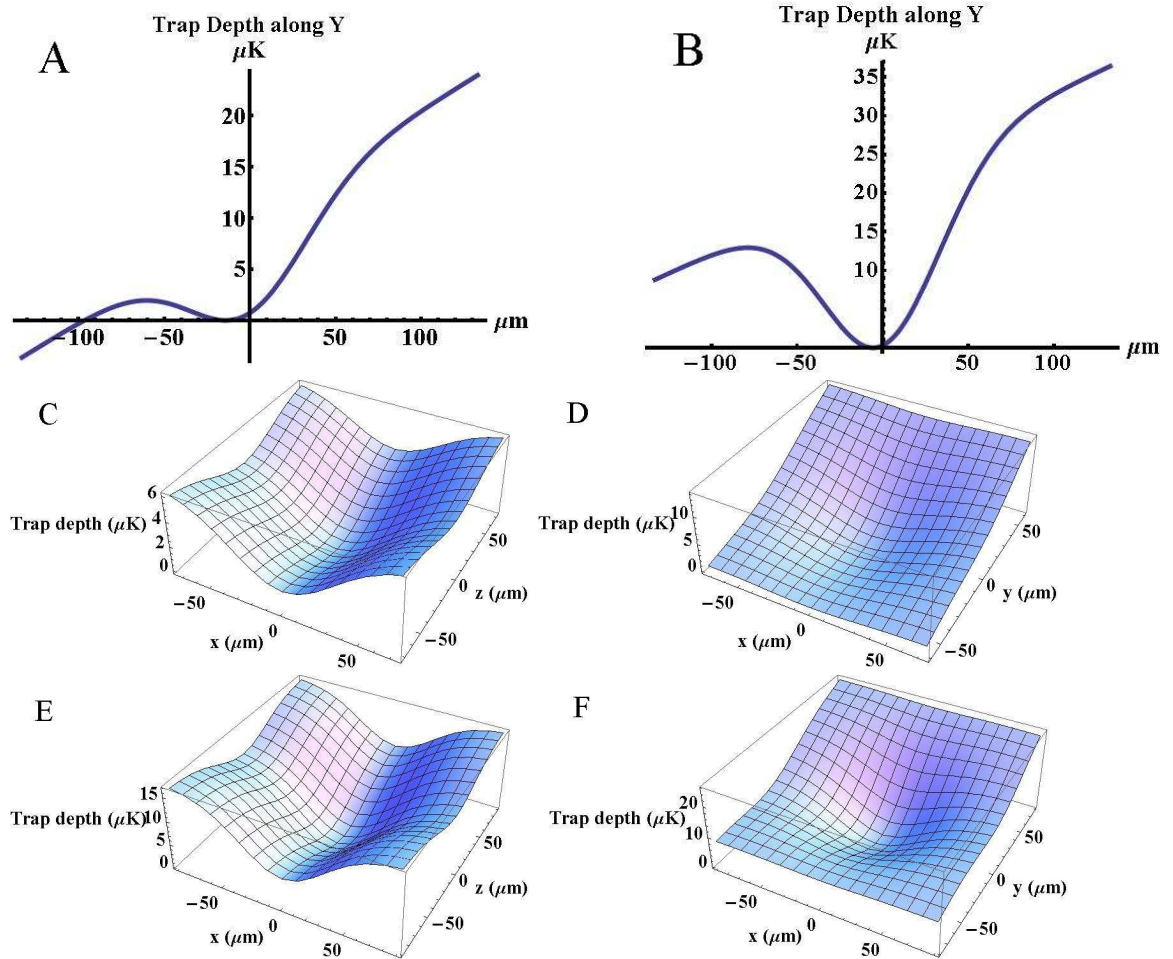


Figure 3.9 : Numerical simulation of loading trap depth. In the calculation the laser beam waists are the best fit waist. [A] and [B] show the trap potentials in the gravity axis (Y) versus displacement in horizontal direction for both shallow trap (0.65W) and deep trap (1.53W); [C] and [D] present the 3D plots of 0.65W trap depth in vertical (y) and horizontal direction(z), while [E] and [F] are the related trap depth plots for 1.53W trap.

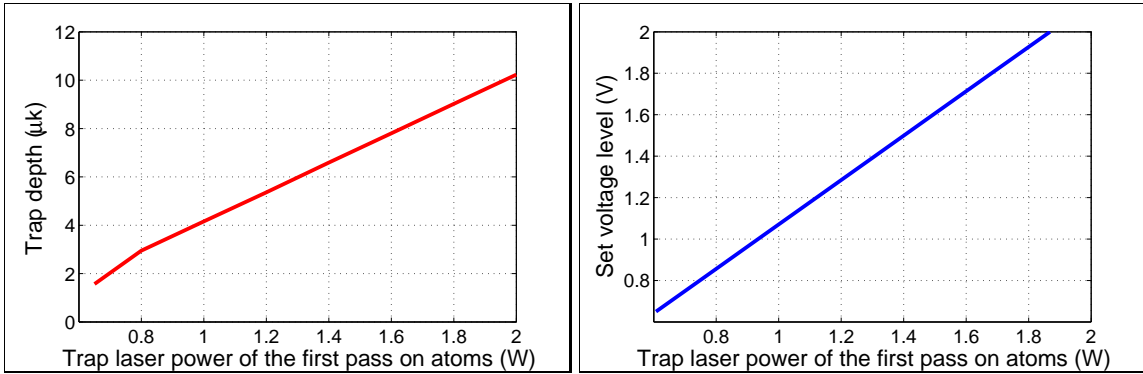


Figure 3.10 : Diagrams of dimple trap power calibration. The left figure presents the trap depth versus first arm dimple trap laser power. As shown the curve is quite linear except a turning point around 0.8W. This is because below 0.8W, the gravity axis determines the trap depth, while at higher power the horizontal saddle points set the potential. The right figure sets the calibration between set voltage and trap power as 0.93V/W.

The large volume in the loading trap keeps down the density of atoms transferred from the final red MOT and reduces the atom loss induced by photo-association process. However, we failed to generate BEC of  $^{88}\text{Sr}$  evaporating in the loading trap alone. We suspect this is because the scattering length between  $^{88}\text{Sr}$  and  $^{87}\text{Sr}$  is not huge and  $^{88}\text{Sr}$  is a parasite on the evaporative cooling power of  $^{87}\text{Sr}$ . As the collision rate  $\gamma = n\delta v$ , where  $\delta = 8\pi a^2$  is the cross-section,  $n$  is the atomic density and  $v$  is the mean free velocity, we'd like to increase the density of atoms during the evaporation process to increase the elastic collision rate, and improve the thermalization efficiency. So we transfer the mixture of  $^{88}\text{Sr}$  and  $^{87}\text{Sr}$  from the large volume loading trap into the dimple trap, which squeezes the atom cloud into a tight volume. The higher density will also allow us to reach BEC at a higher temperature.

In the experiment, we first load  $^{88}\text{Sr}$  and  $^{87}\text{Sr}$  for 200ms and 8s respectively to yield

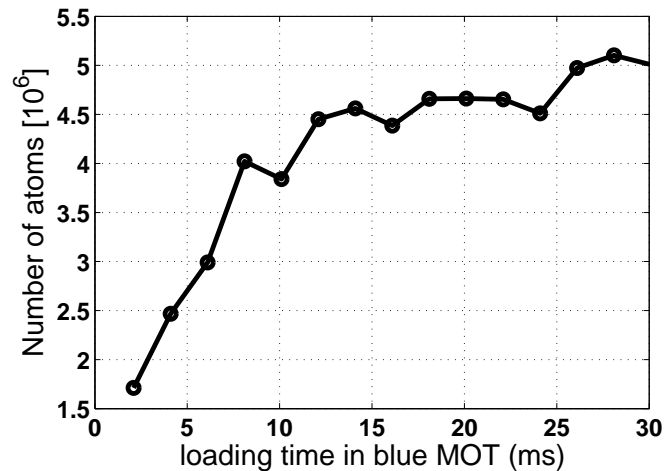


Figure 3.11 : Loading curve in dimple trap for  $^{87}\text{Sr}$ . Hold in dimple trap for 100ms.

equivalent numbers of either isotopes in the loading trap, and then evaporatively cool the sample by decreasing the loading trap power from 7V to 2.8V over 1s. During this same time, we linearly ramp up the dimple laser power to 2V and adiabatically transfer atoms from the loading trap into the dimple trap as the temperature drops down, and abruptly turn off the loading trap. Finally we perform a slow evaporative cooling trajectory in the dimple trap for 4s and Bose-Einstein condensate of  $^{88}\text{Sr}$  has been observed. Figure 3.12 shows the optimized evaporation trajectory in the combined optical trap to give best sympathetic cooling efficiency.

Figure 3.13 shows the time-of-flight image of the atom cloud after a full evaporation of 5s. We fit the thermal part of the atom cloud by the Bose-Einstein distribution and the condensate part by the Gaussian distribution (Figure 3.14). The total BEC number is 8800 at the temperature of 117nk, and the BEC fraction is 7%, and the peak density is on the order of  $10^{15}\text{cm}^{-3}$ .

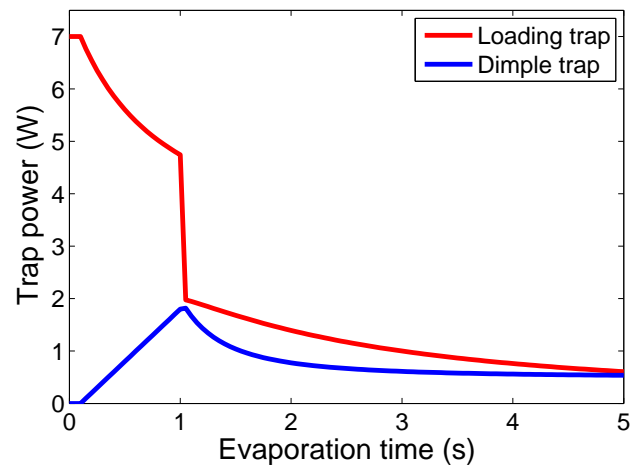


Figure 3.12 : Evaporation trajectory for  $^{88}\text{Sr}$  in the optical dipole trap.

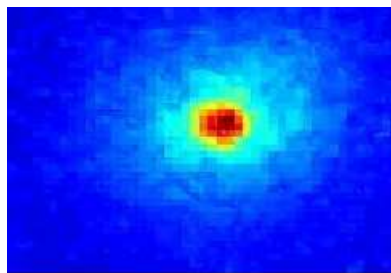


Figure 3.13 :  $^{88}\text{Sr}$  condensate time-of-flight absorption images.

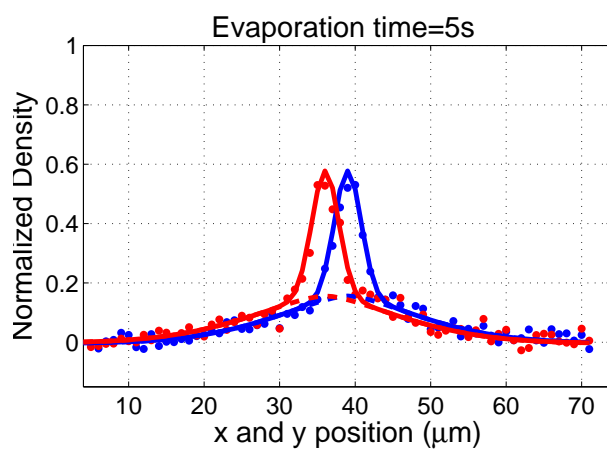


Figure 3.14 : Bimodal distribution fitting of  $^{88}\text{Sr}$  thermal cloud and condensate.

## Chapter 4

### High aspect radio sheet trap to produce $^{86}\text{Sr}$ BEC

$^{86}\text{Sr}$  has the largest scattering length ( $800a_0$ ) and three-body loss rate  $K_3 = 6(3) \times 10^{24}\text{cm}^6/\text{s}$  [20] in all Strontium isotopes. These collision properties also lead to strong PAS transitions which make this isotope interesting for optical Feshbach resonance experiments. The strong interactions also make it interesting for the study of the correlations induced by strong inelastic interactions. The first BEC of  $^{86}\text{Sr}$  was achieved by the Innsbruck group in 2010 [20]. In April 2013, we successfully created Bose-Einstein condensate of  $^{86}\text{Sr}$  in a newly built optical sheet trap, which paved the way for planned experiments of creating spatial correlations of  $^{86}\text{Sr}$  BEC due to the dissipative interactions in a 3D optical lattice [8]. In this chapter, I will talk about the concerns of designing the appropriate optical trap for evaporative cooling  $^{86}\text{Sr}$  atoms. The optical layout and power locking systems are very similar to the dimple trap system and will not be emphasized here. Finally I will describe the procedure to search for an optimum evaporation trajectory of  $^{86}\text{Sr}$  and show the evidence of observation of  $^{86}\text{Sr}$  BEC in the sheet trap.

## 4.1 Motivation to design an elongated optical trap for generation of $^{86}\text{Sr}$ BEC

Large scattering length can provide high thermalization rate during evaporative cooling, but will also increase the inelastic three-body loss rate as it scales as  $a^4$ , which is detrimental to efficient evaporation efficiency. It is important to restrict the effect of inelastic collision by either tuning the scattering length to a lower value or keeping the atomic density low, as the three-body recombination rate is also proportional to  $n^2$  [19]. One possible way to control the scattering length for alkaline-earth atoms is through optical Feshbach resonance, but this has not been investigated in details and is likely to induce photo-association loss. We have explored the solution of keeping the density low at all times. The estimate loss time in  $^{86}\text{Sr}$  BEC due to three-body recombination for a peak density as  $n = 10^{12}\text{cm}^{-3}$  is  $1(0.3)\text{s}^{-1}$  [20]. However, for low densities, the transition temperature will be very low. So we have to evaporatively cool to low temperatures and gravity becomes a problem unless the confinement of the optical trap along the gravity axis is very tight. In our experiment we designed a sheet-shaped optical dipole trap which has an aspect ratio as 1:10 vertically to horizontally, which yields a relatively large effective volume while keeping a tight confinement against gravity. Another concern of the efficiency of the evaporation in the trap is the hydrodynamic limitation, where the collision rate is much larger than the oscillation frequency of the harmonic trap [2]. We tried to generate BEC of  $^{86}\text{Sr}$  in the dimple trap which has a  $60\mu\text{m}$  waist unsuccessfully. We suspect the

hydrodynamic effects were limiting us, so we decided to implement a  $30\mu\text{m}$  vertical waist sheet trap to get out of the hydrodynamic regime.

## 4.2 Description of trap design

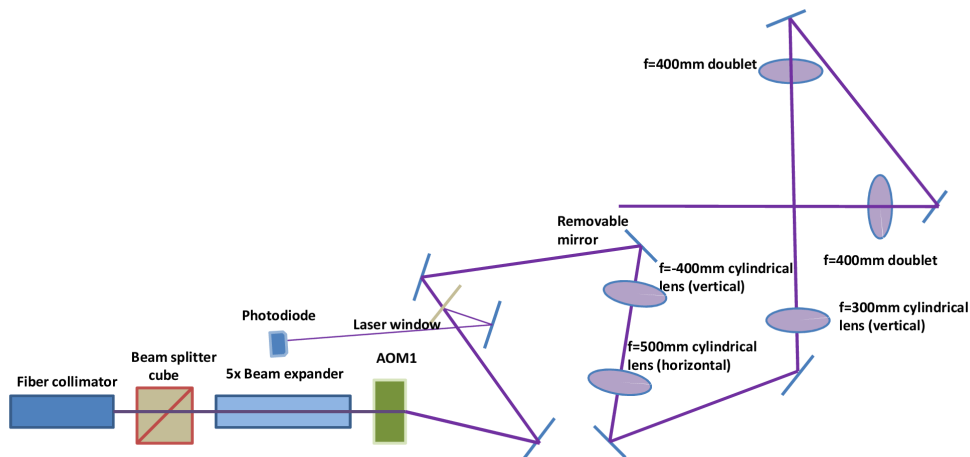


Figure 4.1 : Schematics drawing of sheet trap optical layout.

The sheet trap shared the same laser and optics as the dimple trap until just after the AOM and power control. As they will never be used at the same time, for the sheet we have a removable mirror that reflects the power to the sheet path. We have a single  $f=500$  mm cylindrical lens at 111cm with respect to the fiber collimator output front that forms a very large waist in the horizontal direction. For the vertical axis, we use an  $f=-400$  mm cylindrical lens at 105cm to expand the beam and then an  $f=300$  mm cylindrical lens at 181cm to make a very tight waist. All the absolute

distances have the same origin at the fiber collimator output edge. As the alignment in the vertical direction is very critical, we mount the second cylindrical lens on an x-y rotatable translator mount on a z linear translation stage, which gives the freedom for adjustment in all 4 axes. The design for the horizontal axis of the beam is not critical and only a loose confinement of atoms is required, and the size in this axis was chosen to match the size of the atoms in the red MOT roughly. We also take use of the recycled beam by co-aligning the first pass of the sheet trap with the counter-propagating loading trap beam. The 8f optical system for the loading trap will also image the beam of the sheet trap crossed on itself. But we did not characterize the return beam to establish whether the waist falls on the atoms (Figure 4.1). Figure 4.2 showed the profile of the first pass of the sheet trap, where the atoms are at 180cm with respect to the origin.

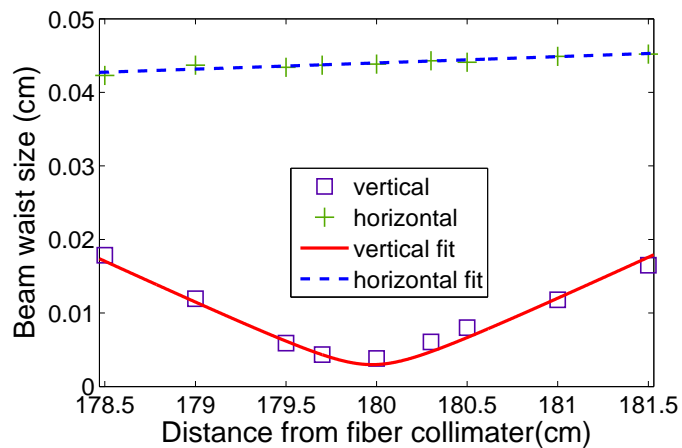


Figure 4.2 : Profile of the first pass sheet trap beam. The horizontal fit waist is  $295.84\mu\text{m}$  at  $151.60\text{cm}$  and the vertical fit waist is  $29.77\mu\text{m}$  at  $179.98\text{cm}$ . Origin is at the fiber collimator output surface.

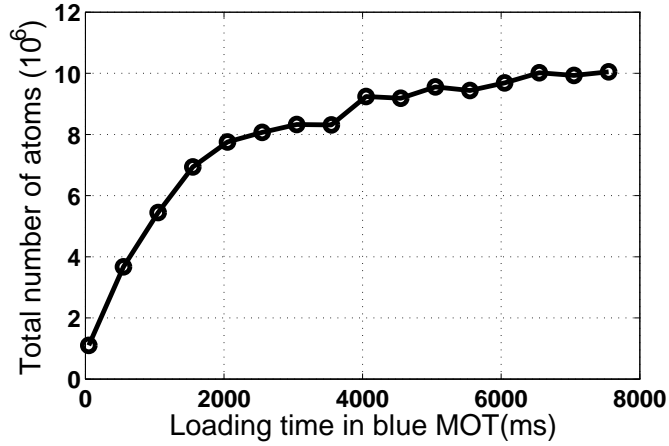


Figure 4.3 : Loading curve in the sheet trap for  $^{86}\text{Sr}$

### 4.3 Achieving $^{86}\text{Sr}$ condensate in a sheet trap

We studied the loading properties of the sheet trap for  $^{86}\text{Sr}$ . We are able to load  $10 \times 10^6$  atoms in 5s and the loading rate saturates at 7s (Figure 4.3). It was found that loading into the sheet was efficient enough that the loading trap is not necessary.

In order to optimize the evaporation efficiency, we varied the evaporation trajectory parameters. The trap potential we performed has an expression as  $V = V_1 / ((1 + (t/\tau))^\beta) + V_2$ , where  $\tau$  determines the evaporation time scale and  $\beta$  defines the specified trajectory. We varied  $\tau = 0.5$  to  $0.125$  and  $\beta = 1.2$  to  $1.4$ . To compare the evaporation efficiency for different trajectories, we choose cooling times  $t$  to yield the same trap depth at the end of evaporation for all the trajectory scans. This led to approximately the same sample temperature at the end of evaporation and made comparison easier. Relatively short evaporation time should be expected

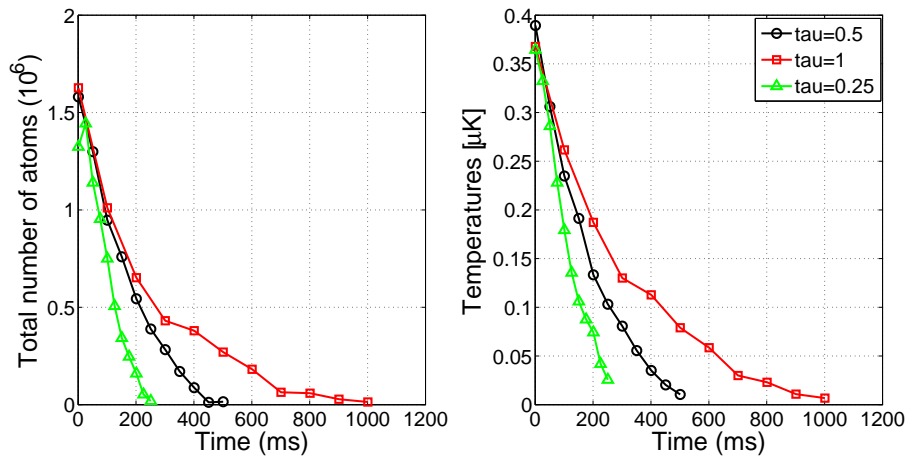


Figure 4.4 : Atom numbers and temperature versus evaporation time for varies evaporation trajectory in the sheet trap for  $^{86}\text{Sr}$ , where  $\beta=1$ .

for cooling  $^{86}\text{Sr}$  compared to other isotopes because of its large elastic collision rate, which leads to high thermalization rate but also high atom loss rate due to three-body recombination.

Figure 4.4 plots out the atom numbers and temperature of atom clouds versus time for three different evaporation trajectories. The atom numbers for all three evaporations reach the same value in the end of the process, while the trajectory with the largest time constant ( $\tau=1$ , red curve) ends up with lower temperature, which leads to a higher phase-space density. However, the atom loss curve for the trajectory with  $\tau=1$  has a very fast atom loss rate before evaporation time of 300ms and then it suddenly slows down. Take this into account, the evaporative trajectory we used to generate Bose-Einstein condensate is shown in Figure 4.5. Firstly we hold the

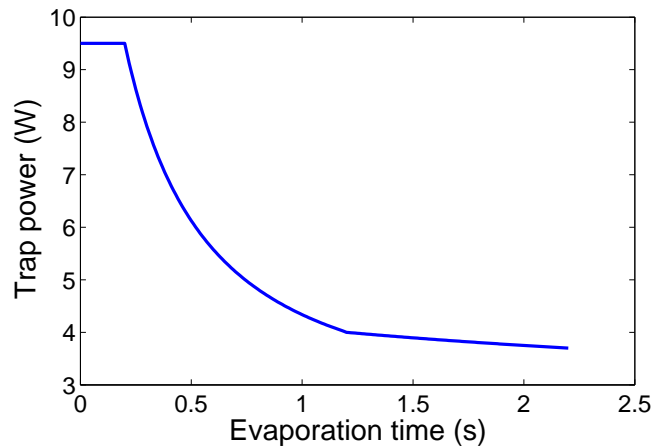


Figure 4.5 : Evaporation trajectory to reach Bose-Einstein condensate of  $^{86}\text{Sr}$

atoms in the trap for a plain evaporation of 200ms and perform a fast evaporation with  $\tau=0.5$  for 1s, then reduce the time constant from 0.5 to 4 which slows down the evaporation process. Figure 4.6 displays the absorption images of the atom clouds during evaporation and the size of the clouds keeps shrinking and the central peak gradually becomes prominent. We fit the condensate by Thomas-Fermi function and the bimodal distribution appears at the evaporation time of 1250ms, which is a sign of accumulation of  $^{86}\text{Sr}$  BEC (Figure 4.7). The transition temperature is around 20nK and the total number of atoms in the BEC is 5500. In our cylindrical optical trap, a signature of formation of Bose-Einstein condensate is the inversion of the aspect ratio of atom clouds in the time-of-flight images, which is conspicuously demonstrated in Figure 4.8. Recent improvements of loading efficiency into the trap have allowed us to create pure condensates with 20,000 atoms.

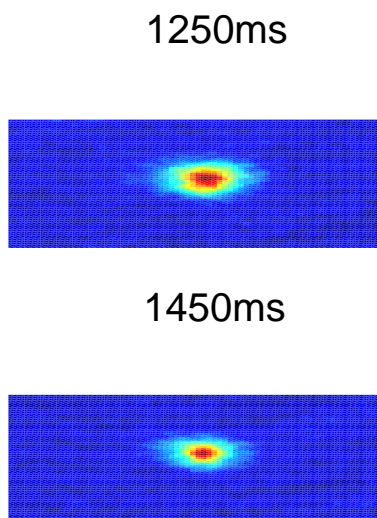


Figure 4.6 :  $^{86}\text{Sr}$  absorption images for different evaporation time.

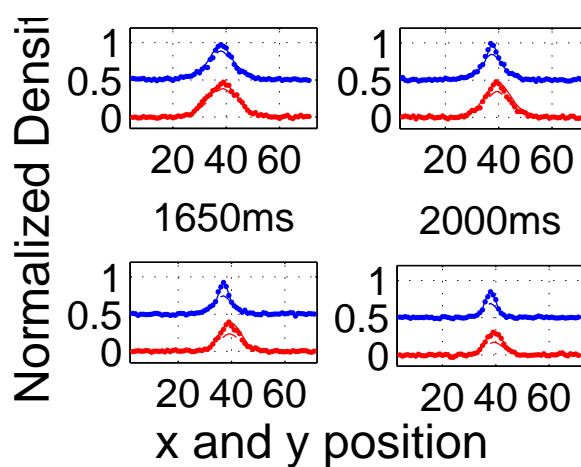


Figure 4.7 : Bimodal distribution fitting of  $^{86}\text{Sr}$  thermal cloud and condensate at different evaporation time. The red/blue dots are the normalized atomic density in x/y directions from experiment. The red/blue solid curve are the Thomas-Fermi fitting for the atom density profiles, while the dashed curves related to the Boltzmann distribution.

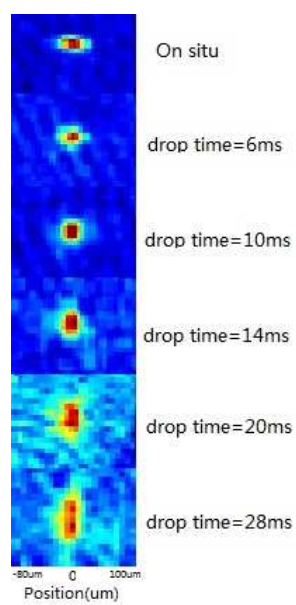


Figure 4.8 : Time-of-flight images of  $^{86}\text{Sr}$  atom cloud after evaporation cooling.

## Chapter 5

### Conclusion

In my master thesis, I demonstrated our new improvements made on the optical dipole traps. The large volume loading trap allows us to load more atoms into the optical trap, which is an excellent intermediate transfer stage for  $^{88}\text{Sr}$  and  $^{87}\text{Sr}$ . It is also an appropriate trap to create a large number of  $^{84}\text{Sr}$  BEC with high evaporation efficiency. The loading trap becomes the most fundamental optical dipole trap for various applications in our experiment. For the tight focus dimple trap, we've already accomplished the experiment of creating coherent Rabi oscillation between BEC atoms and molecules which relies highly on the high density  $^{88}\text{Sr}$  BEC generated in the trap. Most recently we successfully created  $^{86}\text{Sr}$  BEC in the high aspect ratio sheet trap, which paves the way for future experiments on the strong dissipative interactions of Sr in a 3D lattice.

## Bibliography

- [1] C.J.Foot. *Atomic Physics*. Oxford University Press, Oxford, 2005.
- [2] S. Inouye M. R. Andrews D. M. Stamper-Kurn, H.-J. Miesner and W. Ketterle. Collisionless and hydrodynamic excitations of a Bose-Einstein condensate. *Phys. Rev. Lett.*, 81:500, 1998.
- [3] Yenny Natali Martinez de Escobar. PhD thesis, Rice University, 2010.
- [4] R. Grimm, M. Weidemüller, and Y. B. Ovchinnikov. Optical dipole traps for neutral atoms. *Adv. Atom. Mol. Opt. Phys.*, 42:95, 2000.
- [5] T. Ido and H. Katori. Recoil-free spectroscopy of neutral Sr atoms in the Lamb-Dicke regime. *Phys. Rev. Lett.*, 91:053001, 2003.
- [6] Vladyslav Viktorovych Ivanov. PhD thesis, Van der Waals-Zeeman Instituut, Universiteit van Amsterdam, 2007.
- [7] M. Kitagawa K. Enomoto<sup>1</sup>, K. Kasa and Y. Takahashi. Optical Feshbach resonance using the intercombination transition. *Phys. Rev. Lett.*, 101:203201, 2008.
- [8] Theodor W Hansch M Greiner, O Mandel and Immanuel Bloch. Collapse and revival of the matter wave field of a Bose-Einstein condensate. *Nature*, 419:51,

2002.

- [9] Y. N. Martinez de Escobar, P. G. Mickelson, P. Pellegrini, S. B. Nagel, A. Traverso, M. Yan, R. Côté, and T. C. Killian. Two-photon photoassociative spectroscopy of ultracold  $^{88}\text{Sr}$ . *Phys. Rev. A*, 78:062708, 2008.
- [10] Y. N. Martinez de Escobar, P. G. Mickelson, M. Yan, B. J. DeSalvo, S. B. Nagel, and T. C. Killian. Bose-Einstein Condensation of  $^{84}\text{Sr}$ . *Phys. Rev. Lett.*, 103:200402, 2009.
- [11] P. G. Mickelson, Y. N. Martinez de Escobar, M. Yan, B. J. DeSalvo, and T. C. Killian. Bose-Einstein condensation of  $^{88}\text{Sr}$  through sympathetic cooling with  $^{87}\text{Sr}$ . *Phys. Rev. A*, 81:051601(R), 2010.
- [12] Pascal Gerry Mickelson. PhD thesis, Rice University, 2010.
- [13] K.-K. Ni, S. Ospelkaus, M. H. G. de Miranda, A. Pe'er, B. Neyenhuis, J. J. Zirbel, S. Kotochigova, P. S. Julienne, D. S. Jin, and J. Ye. A High Phase-Space-Density Gas of Polar Molecules. *Science*, 322(5899):231–235, 2008.
- [14] K. M. O'Hara, M. E. Gehm, S. R. Granade, and J. E. Thomas. Scaling laws for evaporative cooling in time-dependent optical traps. *Phys. Rev. A*, 64:051403(R), 2001.
- [15] K. M. O'Hara, S. L. Hemmer, M. E. Gehm, S. R. Granade, and J. E. Thomas. Observation of a Strongly Interacting Degenerate Fermi Gas of Atoms. *Science*,

- 298(5601):2179–2182, 2002.
- [16] Eite Tiesinga Pascal Naidon and Paul S. Julienne. Two-body transients in coupled atomic-molecular Bose-Einstein condensates. *Phys. Rev. Lett.*, 100:093001, 2008.
- [17] M. G. Raizen R. Stock, N. S. Babcock and B. C. Sanders. Entanglement of group-II-like atoms with fast measurement for quantum information processing. *Phys. Rev. A*, 78(25):022301, 2008.
- [18] Bo Huang Rudolf Grimm and Florian Schreck Simon Stellmer, Meng Khoon Tey. Bose-einstein condensation of strontium. *Phys. Rev. Lett.*, 103:200401, 2009.
- [19] Rudolf Grimm Simon Stellmer and Florian Schreck. Production of quantum-degenerate strontium gases. *Phys. Rev. A*, 87:013611, 2013.
- [20] Rudolf Grimm Simon Stellmer, Meng Khoon Tey and Florian Schreck. Bose-Einstein condensation of  $^{86}\text{Sr}$ . *Phys. Rev. A*, 82:041602, 2010.
- [21] Yoshitomo Isoya Tetsuya Ido and Hidetoshi Katori. Optical-dipole trapping of Sr atoms at a high phase-space density. *Phys. Rev. A*, 61:061403, 1999.
- [22] M. Yan, R. Chakraborty, P. G. Mickelson, Y. N. Martinez de Escobar, and T. C. Killian. Numerical modeling of collisional dynamics of Sr in an optical dipole trap. *Phys. Rev. A*, 83:032705, 2011.